MASTERARBEIT / MASTER'S THESIS

Titel der Masterarbeit / Title of the Master's Thesis

„Structure and Relaxation Behaviour of Human Hair“

verfasst von / submitted by

Brigitte Waldmann BEd

angestrebter akademischer Grad / in partial fulfilment of the requirements for the degree of

Master of Education (MEd)

Wien, 2022 / Vienna 2022

Studienkennzahl lt. Studienblatt / degree programme code as it appears on the student record sheet:	A 199 520 523 02
Studienrichtung lt. Studienblatt / degree programme as it appears on the student record sheet:	Masterstudium Lehramt Sek (AB) Lehrverbund Unterrichtsfach Mathematik Lehrverbund Unterrichtsfach Physik Lehrverbund
Betreut von / Supervisor:	Univ.-Prof. Mag. Dr. Herwig Peterlik

Contents

1 Introduction

Human hair plays an important role in our modern society, either as a symbol for a specific lifestyle or as an attribute to beauty. Consequently, the cosmetic industry has a great interest in developing hair care and styling products for various desires. In order to produce qualitative goods it is essential that the effects of hair products can be evaluated. For this purpose, first the properties of natural hair have to be studied. Secondly, the effects of the treatment with a specific styling product can be analysed.

When considering popular leisure time activities, it is apparent that hair is subjected to numerous impacts in daily life. Among others, these range from UV-light exposure over extreme temperatures and temperature changes to exposure to chlorine or salt water. Additionally, daily hair care routines and special styling techniques have a great influence on hair. This includes simple care processes such as brushing and shampooing as well as actions like colouring, bleaching or curling hair. For a profound investigation of properties of hair and its reaction to a specific treatment, it is necessary to concentrate on a certain aspect. In this thesis, the focus is put on the mechanical properties of natural hair. In daily life, mechanical stress is frequently applied to hair. This takes place for instance via stroking hair, towelling, straightening or curling hair. It is desired that these treatments do not damage the hair fibre, but that hair stays mechanically stable. Thus, it is of interest which changes occur in hair, when subjected to mechanical stress, and whether these changes are reversible.

The aim of this thesis is to analyse how natural hair reacts when subjected to mechanical tension. Special focus is put on the relaxation behaviour, that is, to discover if hair recovers after the strain is released and if so, on which time scale this takes place. More precisely, this thesis is designed to answer the following four questions:

i. How is mechanical strain divided on the substructures of the hair fibre?

ii. Does recovery take place? If yes, on which time scale does this happen?

iii. What is the effect of repeated straining?

iv. Is there a difference between pseudo-elastic (strains below approx. 2%) and pseudo-plastic (strains above 2%) deformation?

In order to answer these questions an appropriate measurement cycle is designed. The data is evaluated and the results are discussed and compared to prior studies of properties of hair and other biological tissues like collagen in bones and tendons.

Since solely natural hair is investigated in this thesis, findings can serve as a reference for future studies of hair, that was subjected to a certain treatment such as dyeing, bleaching, straightening, etc.

2 Theoretical Background

In this chapter the necessary theory will be introduced. Firstly, the investigated material, human hair, will be described. Secondly, the theoretical background for the measurement technique will be explained.

2.1 Hair

Hair serves several purposes for all kind of mammals. Initially, its main purpose was to protect living beings from cold and wetness. Nowadays, hair plays a major role in fashion and beauty for human beings. As a consequence, the cosmetic industry has a great interest in developing a variety of hair caring and hair styling products. This ranges from shampoos, over hair dyes to styling items such as hair straighteners or curlers. In order to fabricate efficient products, it is essential to consider the properties of hair and to investigate the effects of hair products on the natural fibre. In this thesis, we focus on the mechanical properties of hair at nanostructural level. For being able to interpret data correctly, it is necessary to have basic knowledge about the main features of hair and its morphology. This will be described in the following section.

Human hair shows a wide variety of different appearances. Diversity is both noticed in the hair colours as well as in the form. Hair shapes differ strongly, varying from straight to curly and even kinky. These appearances can be attributed to the form of the cross-section of hair fibres. Usually, three types of hair are distinguished. There is the caucasian type which varies from wavy to curly in its appearance. Hair of this type typically shows an oval cross-section that slightly varies along the fibre. This type of hair is typical in Europe and Northern America. The asian (or oriental) type shows mainly straight fibres. Its cross-section is rather circular, the whole fibre being approximately cylindrical. Finally, the african type displays very curly and even kinky hair. This is caused by hair fibres that show strong irregularities in diameter. Generally, african hair shows less resistance towards stretching and breaks more easily than other hair types (cf. [1, p. 1]).

Concerning the biological composites, hair can be described as a proteinaceous fibre consisting basically of keratin. The diameter of hair ranges from 50 - 100 μm. Hair shows a strongly hierarchical structure, as described in the following. A schematic picture of this composition is shown in Figure 2.1. Roughly, a hair can be thought of a cylinder that is composed of three clearly distinguishable areas.

The outermost, rather thin layer is the cuticle. It is made up of plate-shaped shells that are arranged in an overlapping manner like roof shingles. The cuticle protects the hair from environmental impacts like water. This region of the hair contains also lipid layers and granules, resulting in fatty protective coating. However, it is not entirely sure where these lipids are exactly located or in which form they might be present, most likely in bilayers or granules (cf. [2, pp. 1284–1285]).

The main part of the hair is the cortex which is hierarchically structured. The cortex consists of several cortical cells of approx. 2 μm in diameter and a surrounding matrix. Each cortical is made up of five to eight macrofibrils that have a diameter of approximately 200 nm. Each of these macrofibrils consists themselves of 500 to 800 intermediate filaments (in the following IFs) surrounded by an amorphous matrix. IFs are sometimes also called microfibrils. The diameter of intermediate filaments ranges from approximately 7 - 11 nm. Every intermediate filament is made up of 7 or 8 paired protofilaments. Each of these is a tetramer which consists of two coiled coils, where each coil is made up of two α-helices of keratin. So, each protofilament shows a four chain structure. Additionally, intermediate filaments show an axial staggering of a length of approximately 6 - 7 nm. It is not absolutely clear where this staggering arises from. It might be a stacking of the tetramers caused by the chemical sequences in the α-helices. Also, it is not clarified how the lateral organization of IFs works and if this might have effects on the axial staggering (cf. [2, pp. 1283–1285]).

Finally, at the core of the hair fibre, there is the medulla, a hollow space in the hair fibre. For human beings the medulla is typically very small and sometimes even nonexistent (cf. [2, p. 1285]).

Since the dimensions of substructures in hair vary from the keratin chains of 1 nm to the whole fibre of diameter of 100 μm, different measurement techniques are necessary to investigate the respective structures. Appropriate techniques are indicated at the top of Figure 2.1. In this thesis the choice of measurement technique

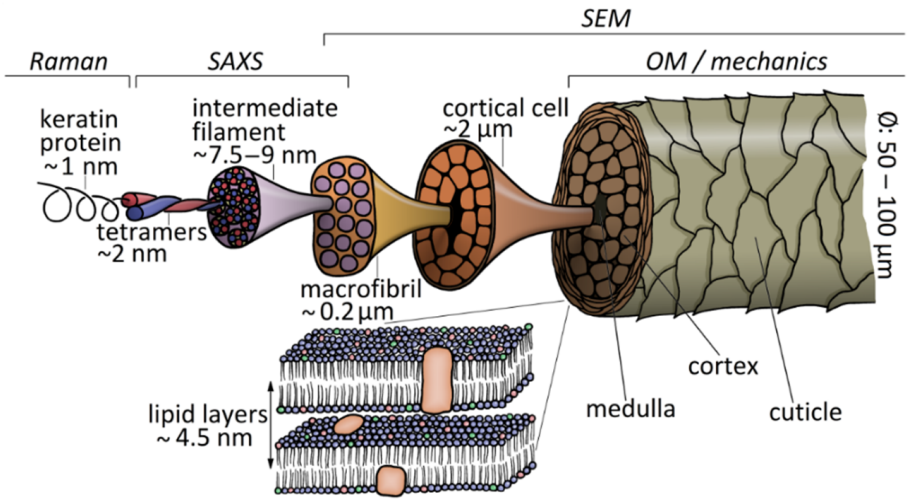

Figure 2.1: Hierarchical structure of hair, by courtesy of Alexander Müllner [4, p. 2]

is small angle X-ray scattering (SAXS), which will be described in more detail in the below section 2.2. With SAXS, structures in the range of 1 - 100 nm can be resolved. Thus, the investigable structures are the lipid layers of size of approximately 4,5 nm, the diameter of IFs or more precisely the centre-to-centre distance of IFs of about 7 - 11 nm as well as the axial staggering of molecules along the IFs, which is in the range of 6 - 7 nm (cf. [3, pp. 109–111]).

2.2 SAXS - Small Angle X-Ray Scattering

In this thesis human hair samples are investigated via means of small angle X-ray scattering (SAXS). In the following the background of this measurement technique is presented. After a short description of X-rays, the basics of scattering are explained, followed by details for the specific case of interest – small angle scattering with X-rays.

2.2.1 X-rays

X-rays are electromagnetic waves with wavelengths ranging approximately from 10^{-8} m to 10^{-12} m. This means that X-rays have typically more energy than ultraviolet light, but less energy than gamma rays. However, this often used description should be taken with caution, because the boundaries between different types of electromagnetic radiation are not sharp. E.g. X-rays produced via synchrotron radiation might have smaller wavelengths than certain gamma rays.

X-ray Spectrum

The spectrum of X-rays can be divided into two parts according to their origin.

On the one hand, X-rays are emitted when charged particles are either rapidly accelerated or decelerated. This process leads to a *continuous spectrum*. Because of its origin this spectrum is also called '*Bremsstrahlung*', which would translate from German to English as 'deceleration radiation' (cf. [5, pp. 4–6]).

On the other hand, there is the so-called *characteristic spectrum*, which is composed of specific discrete wavelengths. This kind of radiation is the result of inner atomic processes. To understand this phenomenon it is important to keep in mind that electrons in an atom can only have discrete energies. It is sufficient to assume that electrons lie in discrete shells each corresponding to a certain energy level. If a particle (typically an electron) with high enough energy hits an atom, it can excite an electron of a low shell into a higher shell. So, in the lower shell there remains a vacancy, which is immediately filled by an electron of a higher shell. As a consequence, the electron has now less energy than before the change of the shells. In the case of inner electrons close to the core, this energy difference is emitted in form of X-rays. Since the energies corresponding to the different shells are well defined and characteristic for each atom, the resulting X-rays are of well defined wavelengths, too. Due to the fact that excitation of electrons from various shells is possible as well as the filling of the vacancy is possible by any of the other shells, the characteristic spectrum is composed of several discrete wavelengths. However, some transitions are more likely than others. Therefore, the intensity of the emitted X-rays depends on the wavelength (cf. [5, pp. 7–10]).

Typically, an X-ray source emits both the continuous and the characteristic spectrum. However, it is important to notice that the intensity of the characteristic spectrum is clearly higher than the intensity of the continuous spectrum (depending on the shells involved, up to 90 times higher). Still, different lines of the characteristic spectrum might be emitted simultaneously by one source. For scattering experiments it is often necessary to have a purely monochromatic beam. In order to achieve this, filters for X-rays can be used. For this purpose materials are used that have an absorption edge for X-rays that lies closely below the desired wavelength. In this way, all other characteristic lines are suppressed and the result is an almost monochromatic beam (cf. [5, p. 18]).

X-ray Sources

To generate X-rays one usually accelerates charged particles. This can be achieved in two ways. Firstly, electrons can be rapidly decelerated in so-called X-ray tubes. Secondly, charged particles that move at a very high velocity can be deflected, as it is the case in synchrotrons.

X-ray tubes are the source of choice for ordinary laboratories, since they are rather small, whereas synchrotrons require a huge facility. All kind of tubes need a source of electrons, a high accelerating voltage and a metal target at which the electrons are decelerated. So, tubes consist of two electrodes. Typically, the target material is the anode which is kept at ground level, whereas the cathode is kept at high negative voltage of about 30 to 50 kilo volts. Nowadays, the source of electrons is usually a hot filament. The emitted electrons are accelerated by the high voltage until they hit the anode, which is the target material. Here, the electrons are rapidly decelerated emitting X-rays of the continuous spectrum as well as of the characteristic spectrum defined by the target material. However, most of the kinetic energy of the electrons is converted into heat. Hence, it is crucial that the target material is cooled sufficiently.

One way to avoid the overheating of the target material and at the same time improving the efficiency of X-ray tubes, which lies at less than 1 percent, is to use rotating anodes. The principle of the X-ray production is the same as for ordinary tubes. Additionally, the anode rotates, so that the electrons do not always hit the target at the same spot. Therefore, the target is not heated as strongly. As a result, higher electron densities are obtained, leading to a greater intensity of the emitted X-rays.

If a very fine X-ray beam is needed, so-called microfocus tubes can be used. These tubes are specially constructed, so that a smaller focus spot of the electrons at the target material is achieved. With suited optics, this results in an X-ray beam with a higher intensity per area.

In order to increase the intensity even further, synchrotron radiation must be used. In synchrotrons charged particles are kept on a curved trajectory. This is typically achieved via the use of magnetic fields. Since the particles move at relativistic velocities, X-rays are emitted when deflecting the particles. Synchrotrons typically have several beam lines which can be used for experiments. The intensity of those X-rays is clearly higher than that of ordinary X-ray tubes (cf. [5, pp. 19–26]).

Besides the intensity and the monochromaticity, another important property of X-rays is the collimation of the beam. For a high resolution of scattering images, a well collimated beam is desired. In order to achieve this, several pinholes or slits are used as a collimation system. For detailed information see e.g. [6, pp. 66–68].

2.2.2 Scattering

In this sections the basic theory of scattering is introduced. Most of the following section is based on the book 'Small-Angle Scattering' by Ian Hamley (cf. [7]).

The term scattering means that the direction of radiation or the direction of motion of a particle is changed due to the collision with a particle. In scattering experiments one analyses these changes of directions, in order to draw conclusions about the object causing the scattering. The basic setup for scattering experiments is a beam of light/X-rays/protons/neutrons/etc. and a detector positioned to measure the deflected beam. Often, the detector is positioned perpendicular to the primary beam line. Then, a specimen is inserted in the beam line and one analyses the resulting scattering image on the detector. Scattering occurs whenever the size of the scatterer is in the size of the wavelength of the used beam. That means, when X-rays are used for scattering experiments, structures in the size of about 10^{-7} m to 10^{-10} m can be resolved, which is roughly the size of atoms and biological structures on the nanoscale.

For being able to interpret scattering images correctly one needs to understand the underlying processes. These are described in the following.

One can distinguish two main scattering processes:

Inelastic Scattering

When there is an energy transfer to the scattering centre, the incoming and the scattered waves are incoherent, since they do no longer have the same wavelength. This means that inelastic scattering can not lead to any interference patterns and is therefore only part of the background radiation in scattering experiments. Furthermore, inelastic scattering accounts only for a small amount of scattered waves in small angle scattering and is therefore negligible for experiments in this thesis (cf. [8, p. 18]).

Elastic Scattering

If the scattering process takes place without any energy transfer, we talk about elastic scattering (also called *Thomson scattering*). In this case the incoming and the outgoing waves have the same wavelength and interference takes place. In order to be able to describe scattering processes, a few terms are needed.

Plane waves can be described mathematically via

$$A_0\, e^{-i\vec{k}\,\vec{x}} \tag{2.2.1}$$

where A_0 is the amplitude and $\vec{k}$ is the wave vector that describes the direction of motion of the wave. For simplicity reasons, the amplitudes of the incident waves will be set to 1 in the following.

The absolute value of the wave vector depends on the wavelength λ

$$\left|\vec{k}\right| = \frac{2\pi}{\lambda}. \tag{2.2.2}$$

Let us describe a scattering process with the variables depicted in Figure 2.2. The direction of the incoming wave is defined by the wave vector $\vec{k}_i$ and the direction of the scattered wave by the wave vector $\vec{k}_s$. The difference of the scattered and the incoming wave vector is called the *scattering vector* $\vec{q}$

$$\vec{q} = \vec{k}_s - \vec{k}_i. \tag{2.2.3}$$

For elastic scattering the relation between the absolute value of the scattering vector q and the scattering angle 2θ can be calculated geometrically. The absolute values of the incoming and the scattered wave vectors are the same, since the wavelength λ does not change for elastic scattering, so

$$\left|\vec{k}_i\right| = \left|\vec{k}_s\right| = \frac{2\pi}{\lambda}. \tag{2.2.4}$$

Calculating the sine in the right angled triangle in Figure 2.2 gives (cf. also [7, p. 3])

$$\sin\theta = \frac{q}{2} \cdot \frac{\lambda}{2\pi}. \tag{2.2.5}$$

Rearranging this formula leads to the absolute value of the scattering vector q

$$q = \frac{4\pi \sin\theta}{\lambda}. \tag{2.2.6}$$

As can be seen from this formula or directly from the sketch in Figure 2.2, large

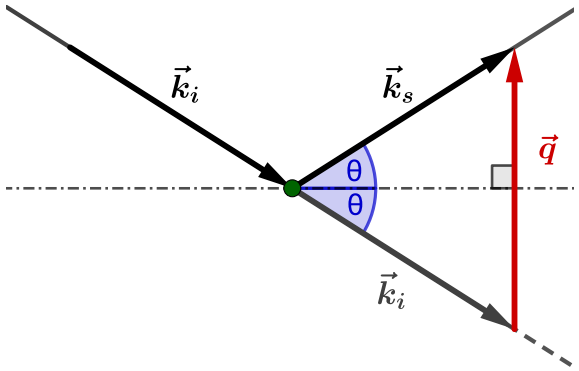

Figure 2.2: Elastic Scattering: Incoming wave with wave vector $\vec{k}_i$, scattered wave with wave vector $\vec{k}_s$, scattering vector $\vec{q}$ and scattering angle 2θ

q-values correspond to large scattering angles 2θ. Since q is proportional to $1/\lambda$, the dimension of the scattering vector q is that of a reciprocal length (m^{-1}).

With these terms and relations in mind one can start analysing scattering images. Since elastic scattering leads to coherent waves, incoming and outgoing waves interfere. So, the scattering pattern is the result of the interference of the incoming beam and all possible scattered waves.

To start with, we consider only one scatterer as depicted in Figure 2.2. Using Equation 2.2.3, the scattered wave $e^{-i\vec{k}_s\,\vec{x}}$ can be obtained mathematically by applying a phase shift via the factor $e^{-i\vec{q}\,\vec{x}}$ to the incoming wave.

In addition, the amplitude of the scattered wave in the direction of $\vec{k}_s$ has to be calculated. This amplitude $f(\vec{q})$ is dependent on the direction and therefore dependent on the scattering vector $\vec{q}$. For its calculation the Huygens-Fresnel principle can be used. That means that each point of the scatterer is the origin of a spherical wave. When the detector is sufficiently far away from the scattering sample those spherical waves can be approximated by plane waves. The resulting scattered wave is the superposition of all those waves. Thus, the amplitude of a wave scattered by an object with spatial density distribution $\rho(\vec{r})$ is given by

$$f(\vec{q}) = \int_V \rho(\vec{r})\, e^{-i\vec{q}\,\vec{x}} d^3r \tag{2.2.7}$$

where the integration range is the volume V of the scattering object. (The density distribution is to be chosen as the density of the particles causing the scattering, e.g., for scattering by X-rays, $\rho(\vec{r})$ is the density distribution of electrons.)

Mathematically speaking, the amplitude of the scattered wave is given by the

fourier transform of the spatial density distribution $\rho(\vec{r})$ of the scatterer. If the scatterer is one atom, Equation 2.2.7 is also called the *atomic form factor* (cf. [9, p. 76]).

Secondly, we consider the scattering by a sample consisting of N identical scatterers, that is, N atoms at positions $\vec{r}_j$ (with $j = 1, \ldots, N$). Here, all waves scattered by the N atoms have to be summed up, for each atom j taking into account their amplitudes f_j calculated via Equation 2.2.7 and their relative phases $e^{-i\vec{q}\,\vec{r}_j}$ (cf. [7, p. 3]). So the total amplitude $A(\vec{q})$ of the scattered wave is given by

$$A(\vec{q}) = \sum_{j=1}^{N} f_j(\vec{q})\, e^{-i\vec{q}\,\vec{r}_j}. \tag{2.2.8}$$

In scattering experiments the amplitude of scattered waves can not be measured directly, but only the intensity is seen on the detector. The measured intensity $I(\vec{q})$ is proportional to the square of the amplitude $A(\vec{q})$ (cf. [7, p. 4])

$$I(\vec{q}) \propto |A(\vec{q})|^2 = A^*(\vec{q}) \cdot A(\vec{q}) = \sum_{j=1}^{N}\sum_{k=1}^{N} f_j(\vec{q}) f_k(\vec{q})\, e^{-i\vec{q}\,(\vec{r}_j - \vec{r}_k)}, \tag{2.2.9}$$

where $A^*(\vec{q})$ denotes the complex conjugate of the amplitude $A(\vec{q})$.

For an isotropic system one can calculate the orientational average. As a result one finds a formula for the intensity depending on the absolute value q. Indicating the orientational average by $\langle \cdot \rangle$ this results in

$$I(q) \propto \sum_{j=1}^{N}\sum_{k=1}^{N} F_j(q) F_k(q) \left\langle e^{-i\vec{q}\,\vec{r}_{jk}} \right\rangle, \tag{2.2.10}$$

where $\vec{r}_{jk} = \vec{r}_j - \vec{r}_k$ and $F(q)$ is the scattering amplitude from within one particle, calculated by the orientational average of the atomic form factor

$$F(q) = \langle f(\vec{q}) \rangle = \left\langle \int \rho(\vec{r})\, e^{-i\vec{q}\,\vec{x}} d^3 r \right\rangle. \tag{2.2.11}$$

The orientational average of the exponential term can be calculated as (cf. [7, p. 5])

$$\left\langle e^{-i\vec{q}\,\vec{r}_{jk}} \right\rangle = \frac{\sin(q r_{jk})}{q r_{jk}} = \operatorname{sinc}(q r_{jk}). \tag{2.2.12}$$

Inserting this result in Equation 2.2.10 leads to the Debye equation for a monodisperse system of spherically symmetric particles

$$I(q) \propto \sum_{j=1}^{N} \sum_{k=1}^{N} F_j(q) F_k(q) \ \mathrm{sinc}(q r_{jk}). \tag{2.2.13}$$

Form and Structure Factors

It can be useful to separate the resulting intensity scattered by an ensemble of particles into two kind of terms – on the one hand, the terms resulting from scattering within one particle, and on the other hand, terms resulting from interference processes of scattered waves by different particles. Terms of the first type are called the *form factor* and terms of the latter type are called the *structure factor* (cf. [7, pp. 8–9]).

For the purpose of separating those two parts of the scattered intensity of a monodisperse system of spherically symmetric particles, Equation 2.2.13 is rewritten as

$$I(q) \propto \sum_{j} F_j^2(q) + \sum_{j \neq k} \sum_{k} F_j(q) F_k(q) \ \mathrm{sinc}(q r_{jk}). \tag{2.2.14}$$

Here, the first term with summands $F_j^2(q)$ corresponds to the intra-particle effects. It is the so-called *form factor* $P(q)$

$$P(q) = \sum_{j} F_j^2(q). \tag{2.2.15}$$

Whereas the second term corresponds to inter-particle effects, giving rise to the the so-called *structure factor* $S(q)$, which is defined as

$$S(q) = 1 + \frac{1}{P(q)} \sum_{j \neq k} \sum_{k} F_j(q) F_k(q) \ \mathrm{sinc}(q r_{jk}). \tag{2.2.16}$$

Using those two definitions the total scattered intensity $I(q)$ can be written as the product of the form factor $P(q)$ and the structure factor $S(q)$

$$I(q) = P(q) S(q). \tag{2.2.17}$$

This calculation of the intensity together with the definitions of form and structure factor are helpful for analysing different scattering samples.

Dilute Systems - Form Factor

Samples that are sufficiently dilute do not show any order. For specimens of this kind the inter-particle effects are negligible. Instead, solely the form of the particle defines the scattering pattern. As a consequence, the structure factor $S(q)$ is approximately 1. Thus, the resulting intensity $I_{dilute\,sys.}(q)$ is in good approximation equal to the form factor $P(q)$

$$I_{dilute\,sys.}(q) \approx P(q). \tag{2.2.18}$$

So, the scattered intensity is mainly dependent on the geometrical form of the particles causing the scattering. The form factor can be calculated as the square of the fourier transform of the geometrical shape.

Long Range Order - Structure Factor

Contrarily, the higher the concentration of particles and their ordering, the more important is the structure factor. For extremely ordered samples, such as crystals, the main contribution to the intensity comes from the structure factor. For certain geometries the structure factor can be calculated via approximations, for further information see e.g. [7, pp. 10–14].

In the special case of crystals or similarly ordered structures, the intensity maxima can be determined via Bragg's law. For deriving this equation we consider the following situation: A plane wave hits a crystal with atoms arranged in lattice planes with spacing d. The situation in the plane of incidence is illustrated in Figure 2.3, atoms as black dots, lattice planes as horizontal grey lines, lattice spacing d in blue. The angle of incidence, calculated as the angle between the incoming beam and the lattice planes, is θ. In order to predict the maxima of scattered intensity, Bragg postulated that X-rays are reflected at lattice planes of crystals. This means that the scattering angle is 2θ (see also Figure 2.2).

Intensity maxima occur for scattering angles 2θ for which waves scattered at different lattice planes interfere constructively. In Figure 2.3 only the first two lattice planes are depicted. Constructive interference takes place when the path difference is a multiple of the wavelength λ. Calculating the path length difference via geometrical relations, one obtains Bragg's law

$$2d \sin\theta = n \cdot \lambda, \quad n \in \mathbb{N}. \tag{2.2.19}$$

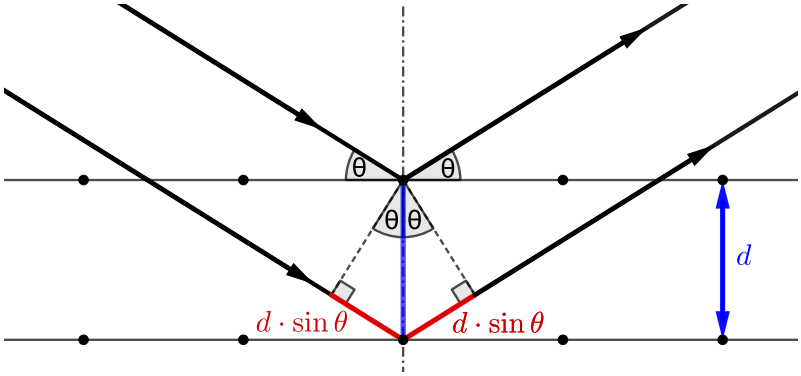

Figure 2.3: Bragg condition for constructive interference: Reflection of incident beam at lattice planes resulting in the scattering angle 2θ.

So, each periodic spacing d in the samples leads to several so-called *Bragg peaks* at an scattering angle 2θ defined by the above equation. However, typically only the first bragg peak ($n = 1$) is in the range of small angle scattering. This means that the layer spacing d in the sample corresponds to a scattering angle 2θ via

$$d = \frac{\lambda}{2 \sin \theta}. \tag{2.2.20}$$

Combining this result with Equation 2.2.6 leads to the correspondence between the layer spacing d in the specimen and the (absolute value of the) scattering vector q

$$d = \frac{2\pi}{q}. \tag{2.2.21}$$

Thus, observing an intensity maximum at a scattering vector q, indicates that the specimen shows a structure with periodicity $d = 2\pi/q$ (cf. [10, pp. 89–91]).

Consequently, small periodic structures d in the sample lead to intensity peaks at relatively large scattering angles 2θ, respectively at relatively large scattering vectors q. Vice versa, large periodic structures result in intensity peaks at small scattering angles and small scattering vectors. In addition, one can notice from Equation 2.2.21 that the scattering vector q has the dimension of an inverse length (m^{-1}). Those two observation give rise to calling the space of scattering vectors q the *reciprocal space*. The ordinary space of structures d in the sample is also called *real space*. For the correct interpretation of scattering images, it is thus essential to keep this reciprocity of distances in mind.

Short Range Order - Both Form and Structure Factor

Some materials do only show a short range order. This is for instance the case, when neighbouring polymers are orientated similarly, and therefore lead to interference patterns, but there is no correlation between polymers that are far apart, so no long range order occurs. For such specimens, it is necessary to consider both the form and the structure factor. As a fibrillar assembly, human hair falls into this category.

For some simple geometries like solid packed spheres, cylinders or lamellar structures analytical expressions are available for the respective form and structure factors, cf. e.g. [7, pp. 11–14]. For calculating the scattered intensity of more complicated specimens, several special models have been developed. For example, the Fischer-Burford model is often used for fractal structures (cf. [7, pp. 20–22]). What is worth noting, is the fact that a fractal dimension D results in a power law behaviour for small scattering vectors q (cf. [11, p. 269])

$$I(q) \propto q^{-D}. \tag{2.2.22}$$

This fact will be used for calculating the scattering background caused by human hair, since this tissue shows a fractal organization of fibrils.

A model especially developed to meet the properties of hair, is the paracrystal model introduced by Briki, Busson and Doucet. With this model, the intensity profile for keratin microfibrils is calculated, modelling the IFs as cylinders that are located at the lattice points of a distorted hexagonal lattice. The output of this fitting model are four parameters: the diameter of the fibrils, their average distance, a distortion parameter of the hexagonal lattice and a scale factor for the scattering background. Despite being developed for human hair, this model can be adapted to any hexagonal fibrillar assembly (cf. [12]).

Unfortunately, this analysis needs very precise data. However, the focus of the experiments in this thesis is on the relaxation behaviour which means that only short measure times are chosen. Consequently, the resulting intensity values are too low to apply the paracrystal model. In order to use this model, synchrotron radiation would be necessary for the performed measurement cycle, which was not possible for this thesis. We therefore focused on the evaluation of the most intense peak maxima.

2.2.3 X-ray Scattering

The wavelength of the beam used for scattering experiments determines which structures can be resolved. Typical wavelengths for X-ray scattering are in the range from $0,5$ Å to $2,5$ Å. This leads to the resolution of structures on the atomic and nanoscale level, that is, approximately the range of 10^{-7} m to 10^{-10} m.

Depending on the resolved scattering angles, one distinguishes between *small angle X-ray scattering (SAXS)* and *wide angle X-ray scattering (WAXS)*.

The term small angle scattering is used for scattering angles 2θ smaller than 5°. According to Bragg's law in Equation 2.2.20, small scattering angles correspond to large structures in the sample. For X-rays this results in the resolution of structures of sizes between approx. 1 nm to 100 nm. Thus, small angle X-ray scattering is a widely used method for analysing the nanostructure of bio-materials.

Contrarily, with wide angle X-ray scattering structures on the atomic level can be investigated, that is, structures around 1 Å $= 10^{-10}$ m. The detected scattering angles typically range from approximately 5° up to 80°. This regime is often also simply referred to as X-ray diffraction (XRD) (cf. [10, pp. 553–556]).

Many of the descriptions in the following apply both to SAXS and WAXS. However, the focus is put on SAXS, since this method is used for experiments in this thesis. Some details in the setup for experiments or the terminology might differ for WAXS applications.

Setup for SAXS Measurements

The basic items necessary for SAXS experiments are: an X-ray source, collimators, a vacuum chamber for the specimen and a detector. For small angle scattering, the source-to-sample as well as the sample-to-detector distance are both rather large, each accounting for approx. 1 m. Because of these large distances, vacuum is essential. Otherwise, the air would reduce the beam intensity too much, because the absorption in the air is too high. In addition, scattering at air molecules would lead to too much background radiation noise.

For SAXS, the source, collimators, pinholes and the beamstop have to be precisely aligned, in order to guarantee a high quality X-ray beam and to protect the detector. The beam is orientated perpendicular to the sample and the detector (cf. [8, p. 37]).

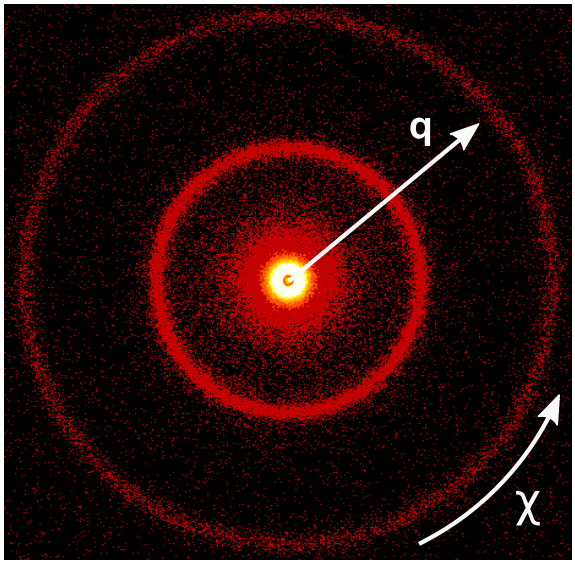

Figure 2.4: Typical SAXS image of AgBH (silver behenate) with the variables scattering vector q and azimuthal angle χ

For more detailed information about the apparatus used for this thesis see also subsection 3.2.1 . The property that defines the intensity of the scattering image is the exposure time. The longer the exposure time, the higher the number of counted photons and therefore more significant results are obtained. However, the number of measurements that have to be performed as well as additional factors such as relaxation effects in the sample restrict the maximum exposure time. Consequently, a compromise of a medium exposure time has to be chosen (cf. [8, p. 53]).

SAXS Scattering Images

An example of a typical small angle scattering image (of silver behenate, AgBH) is shown in Figure 2.4. Scattering images are in general colour coded with light spots corresponding to intensity maxima and dark spots corresponding to intensity minima. For being able to refer to certain points in a SAXS image, typically polar coordinates are used. As shown in Figure 2.4 the scattering vector q corresponds to the radial distance from the centre (and therefore to the scattering angle 2θ via Equation 2.2.6). Whereas, the azimuthal angle χ defines the orientation.

For the interpretation of scattering images, intensity maxima are of special interest. According to Bragg's theory as described above, each intensity peak at a scattering vector q corresponds to a periodic structure $d = 2\pi/q$ in the sample. The orientation of the scattering image is equivalent to the orientation of periodic structures in the specimen. For example an intensity peak in the form of a ring, as

the case for AgBH in Figure 2.4, indicates that the corresponding structure in the sample does not show any favoured orientation. Contrarily, if peaks are only visible for horizontal q-values, the sample shows only a periodicity on the horizontal axis.

For the correct interpretation of scattering images, it is necessary to note that the displayed intensity values are images in reciprocal space. That means that intensity peaks at large q-values correspond to small structures d in real space and vice versa.

For the exact analysis of the scattering images, the first step is to calibrate the sample-to-detector distance as well as the beam centre. This is achieved by first performing a SAXS measurement of a calibration substance whose structure is well known. The position of the intensity peaks are calculated and their theoretical positions and scaling is used to calibrate the measured scattering image. A widely used substance for calibration is silver behenate, AgBH. Its SAXS image is shown in Figure 2.4 (cf. [7, pp. 54–56]).

After this calibration has been performed, scattering images from other samples can be evaluated. Typically, one is either interested in the q-position of a intensity peak or in its azimuthal intensity distribution $I(\chi)$. Thus, the measured data has to be integrated with respect to one of the variables. E.g. to obtain intensity values $I(q)$ only dependent on the scattering vector q, an integration over a sector of a circle (or over a section of a circular ring) is performed

$$I(q) = \int_{\chi_0}^{\chi_1} I(q, \chi)\, d\chi \tag{2.2.23}$$

where χ_0 and χ_1 define the limits of the sector. Now, further analysis, like peak fitting, can be performed with this integrated data (cf. [8, p. 55]).

3 Materials and Methods

In this chapter the prepared specimens of human hair, the used apparatus as well as the experimental setup are described.

3.1 Samples

Hair used for the samples was donated from a European female of age 24. The hair samples have never been dyed or been exposed to any other chemical treatment. Its natural appearance is slightly curled.

From a few strands of hair six specimens were prepared. Only the middle section of the hair was used in order to exlude differences within the hair due to the different age of the hair (near the root or the hair tip) from the evaluation. For the preparation of the samples the hair was cut into pieces of approximately 30 mm. Each specimen is made up from 30 hair pieces. The hair is glued into a paper holder resulting in a strand of hair of the length of 15 mm. The paper strips at the ends of the hair strand are then used to fix the specimen in the experiments.

3.2 Apparatus

For the experiments in this thesis a SAXS apparatus as well as a tensile test machine is necessary. In the following sections the used equipment is described.

3.2.1 SAXS

SAXS measurements were carried out with a Bruker AXS Nanostar equipped with an area gas detector, Våntec 2000. The setup of the saxs apparatus is outlined in Figure 3.1. Its main features are the X-ray source with so-called Montel optics, collimators with pinholes, the vacuum chamber with the sample and the detector. The X-rays are produced by a microfocus tube (IμS high brilliance, Incoatec). The wavelength of the X-ray beam is $\lambda = 1,542$ Å. Its intensity is approximately $2 \cdot 10^8$

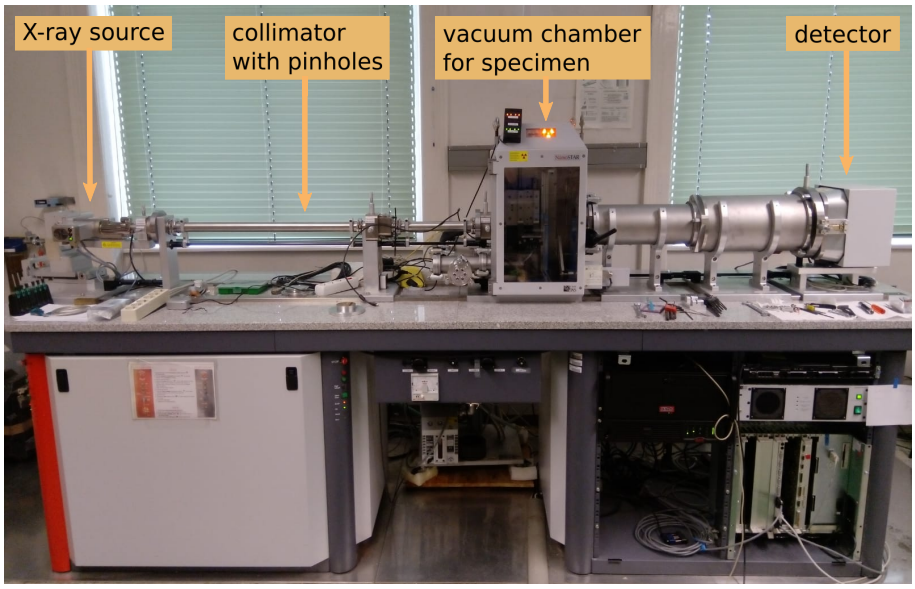

Figure 3.1: Setup of the SAXS apparatus

photons per second and the beam diameter measures 0,5 mm. Since different configurations of the detector can be used, structures from 1 - 100 nm can be evaluated.

All the experiments in this thesis are carried out in the long detector configuration, that is, with a sample-to-detector distance of approximately 108 cm.

3.2.2 Tensile Test Machine

For applying mechanical strain on the specimen, a tensile test machine is used. This apparatus has a sample holder consisting of two clamps. The lower one is fixed whereas the upper one can be moved by a small motor. This motor can be controlled via a computer program connected to the electronic unit (DOLI Elektronik Gmbh). One can manually change the position of the upper clamp via 'up' and 'down' buttons or one can define a position to which the motor moves with a priorly defined speed. All tensile tests in this thesis were carried out with a speed of 0,02 mm per second. A load cell in the tensile test machine measures the load on the specimen. This load as well as the position of the upper clamp can be saved automatically.

3.3 Experimental Setup

In this section the measurement cycle used in the experiments is described. It was designed to meet the goals stated earlier in the introduction (chapter 1). As a recap, the aim of this thesis is to analyse, firstly, which portions of mechanical strain are taken over by the substructures of the hair fibre on the nanoscale, secondly, whether recovery takes place an if so, on which time scale, thirdly, what the effects of repeated straining are, and last, whether there are differences between pseudo-elastic and pseudo-plastic straining. In order to answer these questions the following measurement cycle was designed.

Basically, hair specimens are subjected to tension and their nanostructure is observed via SAXS measurements both before, while and after the tensile tests. The details of the tensile tests and the scattering experiments are described in the following.

The question, which portions of global mechanical strain are visible on the nanostructure of hair, gives rise to the basic measurement cycle. At the beginning, a first SAXS measurement of the natural fibre is performed, that is, with 0 strain on the specimen. Next, the sample is subjected to tension, via straining the hair by 10% of its original length. One specimen followed a different protocol and was only strained by 2%. While keeping the hair under tension, a second SAXS measurement is performed. Afterwards, the strain is released. This is achieved by relaxing the specimen until the load drops to 0, while the strand of hair is still straightened. Due to plastic deformation the hair is at this point longer than in the beginning. However, returning to the original position is not possible since the hair strand has to be straightened and perpendicular to the X-ray beam for the SAXS measurement. At this position a third SAXS measurement is performed. The exposure time is set to 10 minutes for all measurements. With this choice of time, the intensity of the scattered beam is high enough to allow a proper evaluation of the scattering image. However, if the exposure time had been chosen to be longer, strong relaxation effects could not have been avoided. Thus, the analysis of the recovery behaviour would have been distorted.

Summing up, a basic measurement cycle is composed of three SAXS measurements: the first at load 0, the second at load 10% (respectively 2%), and the third again at load 0.

In order to investigate the recovery of hair and at which time scale relaxation takes places, samples have to be strained at least twice with different waiting periods in between the tensile tests. Thus, four specimens undergo two basic measurement cycles with the waiting periods between the two tensile tests varying from 10 min to approximately one week.

Explicitly, the waiting period for the specimen labelled as hair_10min is 10 min, for the specimen hair_1h it is 100 min (which corresponds to approx. 1,5 h), for the specimen hair_1day it is 1000 min (approx. 1 day) and for the specimen hair_1week it is 10 000 min (approx. 1 week). For the shortest waiting period of only 10 minutes, this time span is already over, when the third SAXS measurement of the first tensile test is finished. So, after this measurement the sample is immediately strained a second time. This means only two more SAXS measurements are performed, one at load 10% and another one after the tension was released, again at load 0. In total, five SAXS measurements are performed for the specimen hair_10min.

For the other three samples, six SAXS measurements are performed. When the first basic measurement cycle is finished, the tensile test machine is driven to its original position. The specimen is kept at this unstrained position for the time of the respective waiting period. When this time span has passed, the hair is straightened again with the load still kept at 0. At this position the second basic measurement cycle starts (1. SAXS measurement at load 0, 2. SAXS measurement at load 10%, 3. SAXS measurement at load 0).

In order to analyse the effects of repeated straining, another sample is subjected to several tensile tests. The sample labelled as hair_10 is strained five times in total. The waiting periods in between the tensile tests grow gradually larger. The periods are chosen to be the same as for the other specimens. That means that the first waiting period is 10 min, the second one 100 min, the third one 1000 min and the fourth one 10 000 min. The procedure of both the tensile tests and the SAXS measurements is the same as described above.

Finally, one specimen, labelled as hair_2, is only strained by 2%, so that pseudo-elastic straining can be compared to pseudo-plastic straining. This specimen is subjected to five tensile test, in the same manner as the specimen hair_10.

4 Data Analysis

Human hair shows the typical SAXS scattering image displayed in Figure 4.1a. In this image the hair axis is orientated vertically. The main peaks are highlighted in Figure 4.1b. The innermost peak (marked in black) is caused by the intermediate filaments (IFs). Its position reveals the centre-to-centre distance of the parallel cylinders of the IFs. Usually slight peaks are visible in the region marked in dotted white. These meridional arcs are due to axial staggering of molecules along the IFs. The reason why these arcs are hardly visible in this SAXS image, is the short exposure time of 10 minutes. Nonetheless, the peak is strong enough to be evaluated. The third peak that is indicated in the SAXS image, is a ring coming from lipid bilayers. Since the orientation of peaks in the SAXS image reflects the orientation of the structures within the hair, one can conclude from the ring form of the peak that lipid layers do not show any primary orientation. However, when mechanical strain is applied on the hair one can notice a slight deformation of the ring, resulting in an elliptic shape. This means that lipid layers deform differently depending on their orientation in the hair fibre. Layers that are parallel to the fibre axis turn thinner, when the hair is stretched. Those layers correspond to the horizontal sections of the ring. Layers that are perpendicular to the hair axis are stretched, when strain is applied to the hair. These layers correspond to the vertical sections of the ring. In order to take these effects of the orientation into account, the ring peak is evaluated for horizontal and vertical sections separately. The sections chosen for the evaluation are marked in Figure 4.2b. Vertical sections are highlighted in lightblue, horizontal sections in dashed black (cf. [3, pp. 109–111]).

For the purpose of evaluating the peak positions, one needs to integrate the SAXS data. The two possible integration variables are illustrated in Figure 4.2a. As described earlier in subsubsection 2.2.3 the scattering vector q (or alternatively the scattering angle 2θ) describes the distance from the beam centre. The variable χ describes the azimuthal angle and, thus, the orientation. For experiments in this thesis, only the q-position of the peaks was investigated. Thus, the data is integrated with respect to χ. The result of this integration is a data file with intensity values

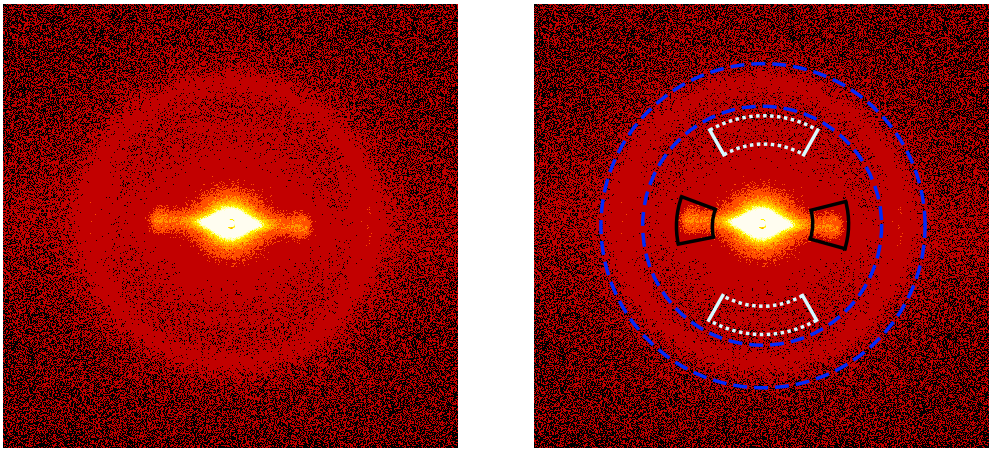

(a) SAXS image of human hair (b) main peaks highlighted

Figure 4.1: Typical SAXS scattering image of human hair in (a). Main peaks marked in (b), from centre of image to periphery: IF peaks from intermediate filaments in black, meridional arcs from axial staggering of molecules within the IFs in dotted white (here hardly visible due to the short exposure time of 10 min), ring caused by lipid bilayers in dashed blue.

$I(q)$ in dependence of the variable q that corresponds to the distance from the beam centre. The integration is performed in four sectors separately, as shown in Figure 4.2a. For each of the sectors, the χ-integration range is set to 30°. This integration range is chosen because it leads to sharp peaks that can be properly evaluated. The orientation of the vertical sectors is chosen to be symmetrical around the hair axis ('meridional axis'). The horizontal sections are achieved by integration over a symmetric intervall around the perpendicular axis ('equatorial axis').

The IF peaks lay within the horizontal sections, whereas the meridional arcs are positioned in the vertical sections. The ring peak appears in all four sections. Still, for the reasons described above, the ring is evaluated separately for the horizontal and the vertical sections.

4.1 Subtraction of the Scattering Background

For the evaluation of the integrated SAXS data the program OriginPro 2018 is used. At the beginning, the scattering background caused by the sample itself has to be subtracted. The two main contributes to the background are the amorphous matrix resulting in a constant intensity and large objects with a fractal size distribution resulting in a power-law scattering (cf. [7, p. 22]).

Firstly, the power-law background intensity $y = c \cdot q^n$ is determined, with the

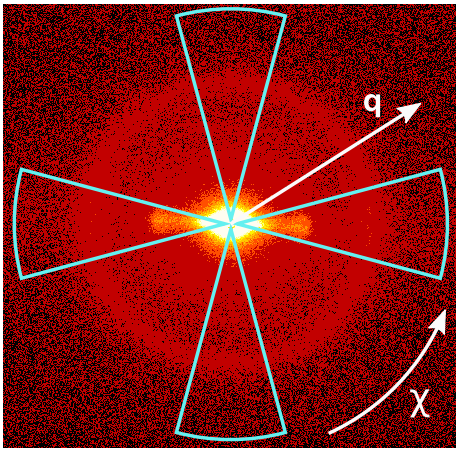

(a) Integration of SAXS data

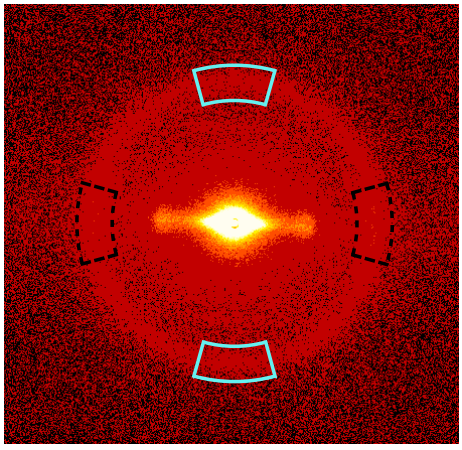

(b) Evaluated sections of the ring peak

Figure 4.2: Integration areas of SAXS data in (a): Integration variables q (respectively 2θ) and χ in white; Areas of integration over χ in lightblue: top, right, bottom and left section.
Separately evaluated sections of the ring peak in (b): vertical sections (caused by layers parallel to the hair axis) at the top and at the bottom, coloured in lightblue; horizontal sections (caused by layers perpendicular to the hair axis) at the left and at the right, coloured in dashed black.

independent variable q and the intensity value y of the power-law component of the background. The parameters c and n are distinguished via a linear fit in log-log-plot of the data, since a power-law transforms to a linear curve in log-log-scale $\log(y) = \log(c) + n\log(q)$ with intercept $\log(c)$ and slope n. The fit range is set to $log(q)$-values from -0,9 to -0,46 (corresponding to q-values from 0,12 nm^{-1} to 0,35 nm^{-1}). This range is chosen, since it is the largest range possible while avoiding the area of the beam stop (small q-values) as well as the area of the peaks (larger q-values). Using the parameters of the linear fit, the power-law baseline is subtracted from the intensity

$$I_{power\text{-}law\ subtracted} = I - c \cdot q^n. \tag{4.1.1}$$

The intensity plot in log-log-scale together with the linear fit can be seen in Figure 4.3a. The fit range is marked in blue, limited by the dashed blue vertical lines. Typical values for the power n vary from -3 to -2. This is in accordance with analysis by other authors, e. g. Briki et al. mention a slope of $n = -2,33$ in their analysis in [12, p. 62].

Secondly, a constant background is subtracted. This background arises from a

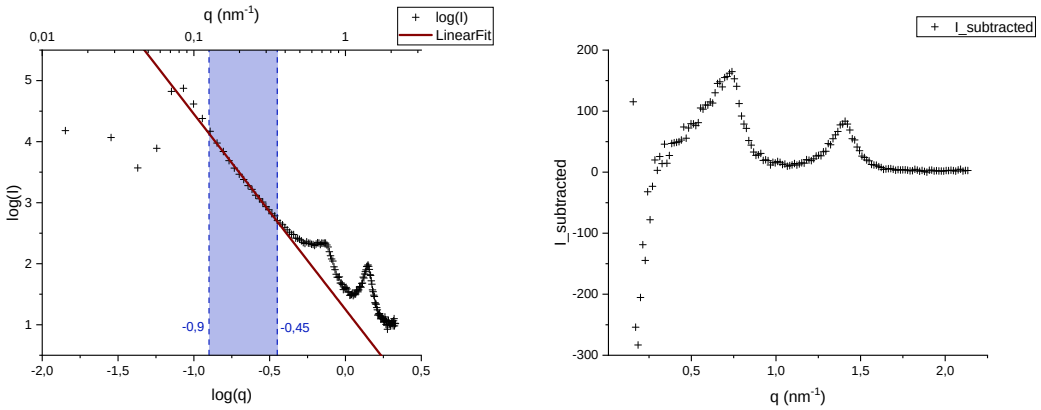

(a) Linear fit in log-log-plot for the power-law baseline; fit area marked in blue

(b) Subtracted intensity of hair_10 before the first extension

Figure 4.3: Determining the power-law background via a linear fit in log-log-plot in (a). Subtracted intensity of hair_10 before the first extension in (b).

purely homogeneous and amorphous matrix. To ensure the best performance of the peak fits, the subtracted data should not contain any negative values. Therefore, the constant background is set to the minimum I_{min} of data $I_{power\text{-}law\ subtracted}$ in the range of the peaks, that is, the last 120 data points (q-values larger than 0,42 nm^{-1}).

So in total, the subtracted data I_{sub} is achieved by subtracting the power-law baseline as well as the minimum of the last 120 data points I_{min}

$$I_{sub} = I - c \cdot q^n - I_{min}. \tag{4.1.2}$$

As an example of the baseline subtraction, the subtracted intensity for the first dataset of hair_10 for the left integration section is shown in Figure 4.3b. (Negative intensity values at small q-values are due to the subtraction procedure in the range of the beam stop.) All further evaluation is done with this subtracted data. (In the following this subtracted data will for simplicity reasons be referred to as intensity I.)

4.2 IF Peak

The peak caused by the lateral distance of intermediate filaments exhibits a slight negative skewness. Since only the peak centre is interesting for the discussion in this thesis, it was at first tried to fit the data nevertheless with symmetric Gaussian or Lorentzian functions. Lorentzian functions performed slightly better than Gaussian

functions. Though, to fit the peak centre well only few data points could have been taken into account. Best results were achieved by setting the fit range to data points with intensity values greater than 65% of the intensity maximum $I_{max,\,IF}$. So, for this evaluation only 10 to 20 data points could have been used for each fit.

In order to improve the fit procedure and being able to enlarge the fit range, skewed fitting functions were tested. For the final evaluation the skew normal distribution was chosen. It was implemented in Origin as a user defined fitting function with formula

$$f(x) = y_0 + A \cdot \frac{1}{\sqrt{2\pi}\,\omega} e^{-\frac{(x-x_c)^2}{2\omega^2}} \cdot \left[1 + \mathrm{erf}\left(\alpha \cdot \frac{x - x_c}{\sqrt{2}\,\omega}\right)\right], \tag{4.2.1}$$

where $\mathrm{erf}(x)$ denotes the error function. The parameters of the fitting function are the offset y_0, amplitude A, centre x_c, width ω and skewness α. The skewness of the data varies from -5 to -2.

The fit range for the skew normal distribution could be extended to all data points with intensity values greater than 25% of $I_{max,\,IF}$. This choice of the fit range means that the data points have to be selected by Y-values. In order to be able to do this automatized, the following procedure was used.

The maximum of the intensity $I_{max,\,IF}$ was calculated by taking the maximum of intensity values in the q-range from 0,4 nm^{-1} to 1,13 nm^{-1}. For determining the final fit range, a first fit with a skew normal distribution was performed in the q-range from 0,3 nm^{-1} to 1 nm^{-1}. Next, the Origin function 'Find X from Y' for fitting functions was used to calculate q-values q_1 and q_2 that correspond to intensity values

$$I(q) = y_0 + 0,25 \cdot (I_{max,\,IF} - y_0) = 0,75 y_0 + 0,25 I_{max,\,IF}, \tag{4.2.2}$$

where y_0 is the offset parameter from the fitting function. (This criterion was chosen because for some datasets taking directly 25% of $I_{max,\,IF}$ led outside of the previous fit range 0,3 nm^{-1} to 1 nm^{-1}. When this happens the automatized analysis procedure fails because the 'Find X from Y'-function cannot give any output.) These two corresponding X-Values q_1, q_2 define the final fit range for the evaluation of the IF peak. A second fit with a skew normal distribution in this range is performed. For skewed fitting functions the centre parameter x_c does not coincide with the peak position. However, for the analysis of scattering images, the maxima of the intensity distribution are relevant, since the peak positions in scattering space correspond to the desired distances in the specimen. Thus, the peak position q_{IF} is determined in the following manner.

OriginPro creates for each fitting function a data set with X- and Y-values of the fit curve, where the difference in X-values between neighbouring data points is smaller than 0,0005 nm^{-1}. First, the maximum $I_{fit,\,max}$ of these fitted intensity values is determined. Next, the corresponding X-value q_{IF} is calculated, which is the desired peak position. The resolution of the fit curve gives rise to an uncertainty in the order of 0,001 nm^{-1} of the peak position.

These analysis steps are performed for all data sets. For each SAXS measurement one achieves two maximum positions, one from the left and one from the right IF peak in Figure 4.1b (peaks marked in black). The positions of those two peaks are not perfectly symmetric due to imperfect calibration of the beam centre and a possible detector tilt angle. To take these errors into account, one takes the arithmetic mean of the peak positions from the left and the right data sets. This arithmetic mean is the final value q_{IF} for the peak position of the IF peak corresponding to the centre-to-centre distance of the IFs.

The uncertainty of the IF peak centre can be estimated by the change of the parameter when varying the fit range, since this has the largest effect on q_{IF} in the whole analysis process. This leads to an uncertainty of approximately 0,003 nm^{-1}. Considering that changes in q_{IF} caused by the straining of the specimen are in the range of 0,02 nm^{-1} for 10% strain and respectively 0,006 nm^{-1} for 2% strain, this evaluation holds significant results.

Two examples of fits of the IF peak with skew normal functions are shown in Figure 4.4.

4.3 Meridional Arc

In contrast to the strong peak of the IFs, the meridional arc shows only a slightly higher intensity than the background and therefore results in a very weak peak. For a higher resolution a longer exposure time would be necessary. However, exceeding the exposure time would also mean that the relaxation behaviour of hair could only be tracked on a larger time scale. Nonetheless, the meridional peak is strong enough to be evaluated, even with the rather short exposure time of ten minutes. Still, fitting the peak is not possible, since for the majority of the data sets fits do not converge due to the weak appearance of the peak. Instead a weighted mean q_m is calculated. The q-values q_k are weighted by the corresponding intensity values $I(q_k)$

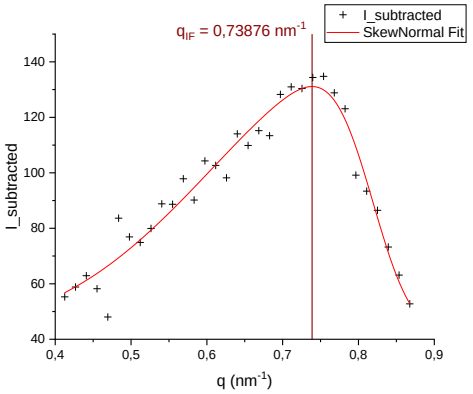

(a) hair_1week at load 10% at second extension (left IF peak)

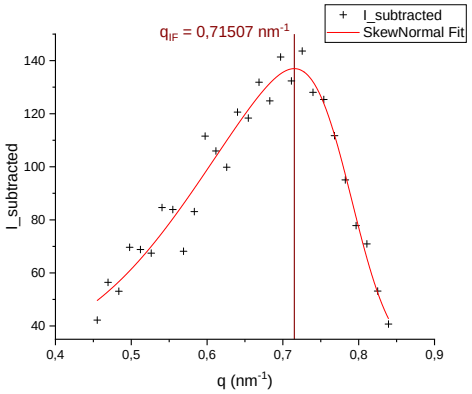

(b) hair_10 at load 0 after third extension (right IF peak)

Figure 4.4: Examples of fits of the IF peak with a skew normal distribution, peak position indicated by vertical line

$$q_m = \frac{\sum_k q_k \cdot I(q_k)}{\sum_k I(q_k)}. \tag{4.3.1}$$

Since the result of the mean is rather strongly dependent on the sum range, a symmetric intervall around the maximum intensity value is chosen. The intervall is taken to be as large as possible while avoiding any overlap with the area of the next peak (from the double lipid ring).

Firstly, the intensity maximum $I_{max,\,m}$ in the q-range from 0,8 nm^{-1} to 1 nm^{-1} is calculated and the corresponding q-value $q_{max,\,m}$ is evaluated. Secondly, the weighted mean is calculated for ten points to the left of $I_{max,\,m}$ to ten points to the right of $I_{max,\,m}$, making in total a weighted sum of 21 data points. The fitting of the calculated value q_m is optically checked by adding a vertical line at position $q = q_m$ to the plot of the intensity I vs. q.

Similarly to the evaluation of the IF peak, for each SAXS measurement two corresponding peaks are evaluated, one for the upper and one for the lower meridional arc. Again, the arithmetic mean q_m of those two values is calculated to eliminate errors due to deviations in the centring of the experimental setup.

The uncertainty of this evaluation is estimated by changes in q_m when the sum range is changed. The size of this effect is around 0,015 nm^{-1}. The peak centre q_m differs by approximately 0,05 nm^{-1} when the sample is strained by 10%. The change

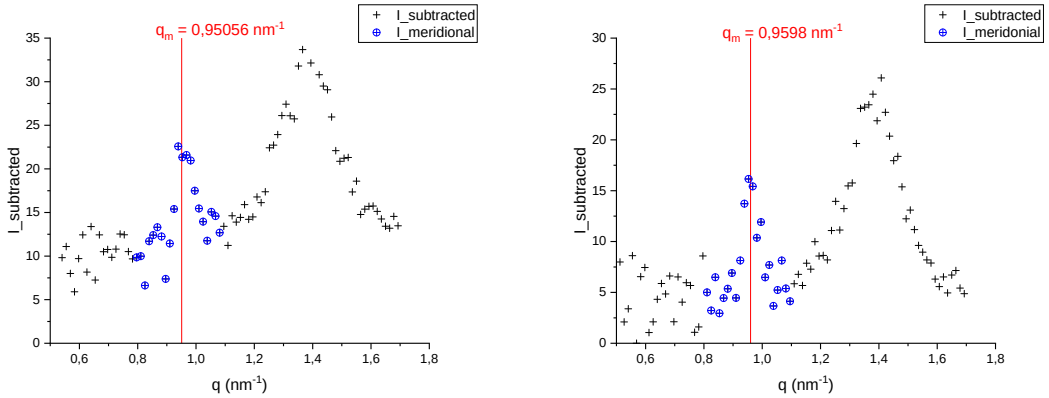

(a) hair_10 at load 0 before fifth extension (upper meridional arc)

(b) hair_2 at load 0 before first extension (upper meridional arc)

Figure 4.5: Examples of weighted mean q_m for meridional arc (red line), range for calculation of weighted mean coloured blue and symbols encircled

for a strain of 2% is only in the range of 0,01 - 0,03 nm^{-1}. Consequently, the findings are significant for extension of 10%, but interpretations for extensions of 2% should be taken with caution, since the uncertainty is for some datasets in the same range as the change due to the extension.

Graphical illustrations of the calculation are shown in Figure 4.5. The calculated mean q_m is indicated by the vertical red line. Data points taken into account in the calculation are highlighted in blue and are encircled. (The peak at approximately 1,35 nm^{-1} corresponds to the double lipids and is only shown for a better assessment of the intensity of the meridional peak.)

4.4 Double Lipid Ring

Data points at the position of the ring peak show a symmetric distribution. Thus, a Lorentzian function is used for fitting, which performed slightly better than Gaussian functions. The fit range is set to all data points with intensity values greater than one third of the maximum intensity $I_{max,ring}$. The same procedure as for the IF peak is performed. This means that firstly, the maximum $I_{max,ring}$ of intensity values is determined in the q-range from 1,2 nm^{-1} to 1,7 nm^{-1}. In order to select the fit range automatically, a first Lorentzian fit is performed for q-values from 1,12 nm^{-1} to 1,63 nm^{-1}. The Origin function 'Find X from Y' is used to distinguish the X-values q_1 and q_2 corresponding to

$$I(q) = y_0 + \frac{1}{3} \cdot (I_{max,ring} - y_0) = \frac{2}{3} y_0 + \frac{1}{3} I_{max,ring}, \tag{4.4.1}$$

where y_0 is the offset parameter of the Lorentzian fitting function. (Again this criterion is chosen instead of directly calculating one third of $I_{max,ring}$ in order to stay within the initial fit range and thus avoiding a collapse of the automatized analysis.) In this new fit range, from q_1 to q_2, the second and final Lorentzian fit is performed.

The peak maximum q_{ring} is determined as the centre parameter of the Lorentzian fitting function.

Similarly to the other peak analysis, in the end the arithmetic mean of maximum positions of data sets left and right are calculated for the horizontal ring sectors. For the vertical ring sectors the arithmetic mean of results from data sets of top and bottom are determined.

Changing the fit range by 5% of $I_{max,ring}$ leads to a difference of the peak centre of 0,0005 nm^{-1} to 0,002 nm^{-1}. Applying a strain of 10% on the specimen causes the peak centre to change by approximately 0,02 nm^{-1}, applying a strain of 2% results in a change of the peak centre by 0,002 nm^{-1} to 0,005 nm^{-1}. Thus, results for strains of 10% are significant. However, for some data sets the strain of only 2% leads to changes in the same order of magnitude as the uncertainty due to the fit.

In Figure 4.6 examples of fits of the ring peak with Lorentzian functions are shown. Both fits are from the same data set, i.e., hair_2 at load 2% in the fifth tension cycle. The left graph shows the evaluation for the right sections of the ring. Whereas, the graph to the right shows the evaluation at the top section of the ring. One can notice the difference in the position of the peak centre of those two sections.

4.5 Correlation of Scattering Data and Real Space Dimensions

To understand the behaviour of human hair when subjected to tension, one needs to analyse the changes of structures in the sample, that is, distances d in real space. However, the experimental data leads to values in reciprocal space. Since these q-values are the direct outcome of data fitting, the analysis of changes due to strain is performed on these reciprocal values q, too. To link findings in scattering space

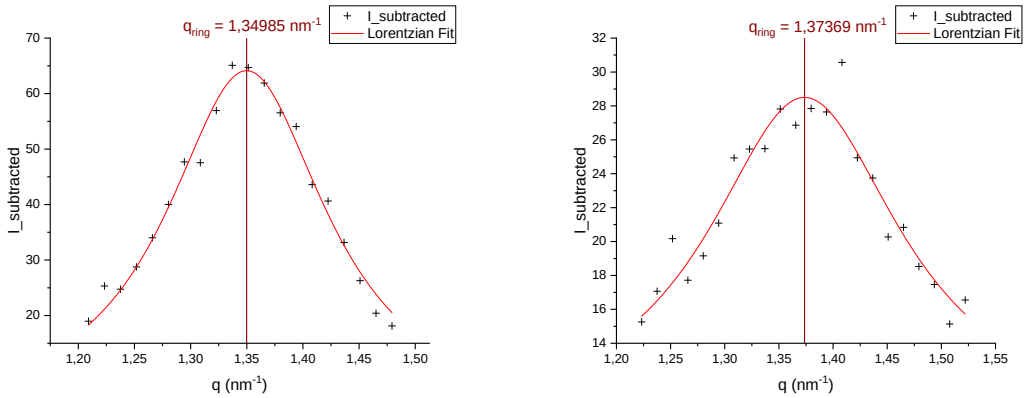

(a) Evaluated for right section of the ring (b) Evaluated for top section of the ring

Figure 4.6: Examples of Lorentzian fits of the ring peak of hair_2 at load 2% in the fifth tension cycle, peak position indicated by vertical line

with distances d in the specimen, it is essential to keep in mind that those two spaces behave reciprocally. A decrease of q-values corresponds to an increase of distances d in the sample and vice versa.

When it comes to relative changes, there is the following relation between reciprocal space and real space dimensions for Bragg peaks. A change factor of q_1/q_0 in reciprocal space corresponds to its inverse in real space

$$\frac{d_1}{d_0} = \frac{1}{\frac{q_1}{q_0}}, \tag{4.5.1}$$

where d_0 is the initial real space value (corresponding to q_0) and d_1 is the final real space distance (corresponding to q_1). The change factor is related to the relative change $\Delta q/q_0$ via

$$\frac{q_1}{q_0} = 1 + \frac{\Delta q}{q_0}. \tag{4.5.2}$$

A relative change of $\Delta q/q_0$ in scattering space translates to a relative change of $\Delta d/d_0$ in the specimen by

$$\frac{\Delta d}{d_0} = \frac{d_1 - d_0}{d_0} = \frac{d_1}{d_0} - 1 = \frac{1}{1 + \frac{\Delta q}{q_0}} - 1. \tag{4.5.3}$$

For small changes $\Delta q/q_0 \ll 1$, this simplifies to

$$\frac{\Delta d}{d_0} \approx 1 - \frac{\Delta q}{q_0} - 1 = -\frac{\Delta q}{q_0}. \tag{4.5.4}$$

Since the changes of q-values observed in this thesis are sufficiently small, the relation above yields a good approximation for changes in the specimen. Hence, a decrease of $p\%$ in the scattering space corresponds to an increase of approximately $p\%$ of real space distances and vice versa. With this simple relation in mind, one can draw conclusions about the samples via analysing the results of q-values.

However, one should bare in mind that these simplified relations hold only for strongly ordered samples, where the Bragg equation defines the maxima in scattered intensity. For less ordered tissues, as it is the case for human hair, objects in real and reciprocal space are related by the fourier transform. Hence, also relative changes in the respective spaces do not transform linearly, but via the fourier transform.

5 Results

For each of the SAXS measurements of every specimen the peak positions q were evaluated for all four peaks (IF, meridional arc, ring horizontal, ring vertical) as described in the previous chapter. As the number of data points is rather large, we decided to present the data in a specific way explained below. This allows an easy comparison of the dependence of each structural feature on time and load cycle.

There is one page of graphs for each peak, resulting in four pages, Figure 5.3 presenting the data for the IF peak, Figure 5.4 for the meridional arc, Figure 5.5 for the horizontal ring section and Figure 5.6 for the vertical ring section. Each page is composed of six subfigures. In every graph, relative peak positions q/q_0 are plotted against the time t, that has passed since the first measurement of the respective specimen. Thus, both relative changes of the peak positions as well as the waiting period between two tensile tests and therefore also the relaxation behaviour are visible. The time scale is chosen to be logarithmic.

The graphs on the left side of each page show the relative changes of peak positions q/q_0 with respect to the peak position q_0 of the first measurement, that is, the peak position of the unstrained, original hair samples. To plot relative values q/q_0 instead of the original evaluation results q, is necessary, because biological tissues show a great variance in size distributions. Thus, even the peak positions of the natural unstrained hair show major differences for different specimens. In order to be nevertheless able to compare findings from different specimens, not the absolute values, but relative peak positions are of interest, as they show a structural change with high precision.

These relative positions for the specimen hair_2, strained by 2%, are shown at the top in subfigure (a), the ones of hair_10, strained by 10%, in the middle in subfigure (c) and the remaining four samples hair_10min, hair_1h, hair_1day and hair_1week, all strained by 10%, are visible at the bottom in subfigure (e). The graphs (c) and (e) for the specimens strained by 10% are plotted in the same data range, so that repeated straining of hair_10 in subfigure (c) can be compared with the samples only

peak (nm^{-1})	hair_2	hair_10	hair_10min	hair_1h	hair_1day	hair_1week
IF	0,7045	0,7082	0,7025	0,6946	0,7047	0,7104
meridional	0,9413	0,9704	0,9521	0,9549	0,9524	0,9563
ring_hor	1,3655	1,3819	1,3741	1,3569	1,3536	1,3676
ring_ver	1,3688	1,3820	1,3704	1,3577	1,3560	1,3666

Table 5.1: Peak positions of first measurements q_0 in nm^{-1} of all six samples

strained twice in subfigure (e).

In those graphs on the left side of each page, both the relative changes of the peak positions and the relaxation behaviour can be seen. To illustrate, whether the nanostructure changes in the same manner when strained and relaxed repeatedly, a different normalization is chosen for the graphs on the right side. In these graphs, the data is normalized anew for each basic measurement cycle by the first SAXS measurement q_{0i} (at load 0) of the respective cycle. For clarity, the three measurements (at load 0, load 10% resp. 2%, load 0) of each cycle are connected by a line. Again, the data of sample hair_2, strained by 2%, is presented at the top in subfigure (b), sample hair_10, strained by 10%, in the middle in subfigure (d) and the other four specimens hair_10min, hair_1h, hair_1day and hair_1week are visible at the bottom in subfigure (f). Also, the scaling in the subfigures (d) and (f) for the samples strained by 10% is the same, allowing the comparison of repeated straining in (d) with samples only strained twice in (f).

As a reference, all peak positions q_0 of the first measurements of each peak and of each specimen can be seen in Table 5.1.

The data points are enumerated in the graphs in the following way. The tensile tests (each composed of three SAXS measurements and, therefore, three data points) are enumerated via 0_*, 1_*, 2_*, 3_*, 4_*. The enumeration within each tensile test is *_1 (for the first SAXS measurement at load 0), *_2 (for the second SAXS measurement at load 10% resp. 2%) and *_3 (for the third SAXS measurement at load 0 again). Combining those two ways of counting gives the sequence of 0_1, 0_2, 0_3 for the first tensile test and 1_1, 1_2, 1_3 for the second tensile test for the specimens hair_1h, hair_1day and hair_1week. When the waiting period is only 10 minutes, the second measurement cycle consists only of the two last SAXS measurements at load 10% resp. 2% and at load 0. Thus, the sequence for hair_10min is given by 0_1, 0_2, 0_3, 1_2, 1_3. Consequently, the enumeration for hair_10 and hair_2 is given by 0_1,

0_2, 0_3, 1_2, 1_3, 2_1, 2_2, ..., 4_3.

As a summary of the numerous data, mean values of the peak positions and the relative changes of positions, when subjected to tension, are calculated. These results are shown in Table 5.2. For each peak the value $\overline{q_0}$ is calculated as the mean of peak positions of the first measurements q_0 of all six specimens. So, this value represents the unstrained natural fibre. The given uncertainty is the standard error, because variances from different specimens are greater than the fitting errors. The corresponding structures $\overline{d_0}$ in real space are calculated via $d_0 = 2\pi/q_0$ (cf. Equation 2.2.21). The uncertainty is calculated via the Gaussian error propagation. In this simple case, this means that the relative errors of q_0 and d_0 are equal.

As can be seen in Table 5.2, the IF peak lays at $q_{IF} \approx 0,70$ nm^{-1} corresponding to the centre-to-centre distance of intermediate filaments of $d_{IF} \approx 8,9$ nm. The meridional arc is positioned at $q_m \approx 0,95$ nm^{-1}, which means that the axial staggering of molecules along the IFs is in the dimension of $d_m \approx 6,6$ nm. The position of the ring peak is in the unstrained case both for the horizontal as well as for the vertical section at $q_{ring} \approx 1,37$ nm^{-1}, corresponding to a lipid bilayer distance of $d_{ring} \approx 4,6$ nm. The peak positions $\overline{q_0}$ in reciprocal space are illustrated in Figure 5.1 (error bars are smaller than the symbols).

In addition, mean values for the relative changes of q-values, when subjected to tension, are calculated. For a strain of 10%, first, the relative changes $(q_1 - q_0)/q_0$ at the first extension are calculated for all five specimens strained by 10%, that is, hair_10, hair_10min, hair_1h, hair_1day and hair_1week. Then the arithmetic mean of those five values is calculated, giving $\overline{\Delta q/q_0}$ as a result. The uncertainty is estimated by the standard error. For a strain of 2%, the relative changes of the five extensions of hair_2 are evaluated and the arithmetic mean of those five values is calculated. Again, the uncertainty is given by the standard error. The relative changes of peak positions in percent are visualized in Figure 5.2. Values for a strain of 10% are depicted as black diamonds, values for 2% strain are shown as red triangles.

It can be noticed that the q-values increase under strain for the IF peak and for the horizontal (equatorial) section of the ring. These two peaks correspond to structures perpendicular to the hair axis and, therefore, perpendicular to the tension axis. Considering the reciprocity between q-values and distances d in real space, this means that the corresponding d-values decrease. Contrarily, q-values decrease for the meridional arc and for the vertical (meridional) sections of the ring. Thus, the

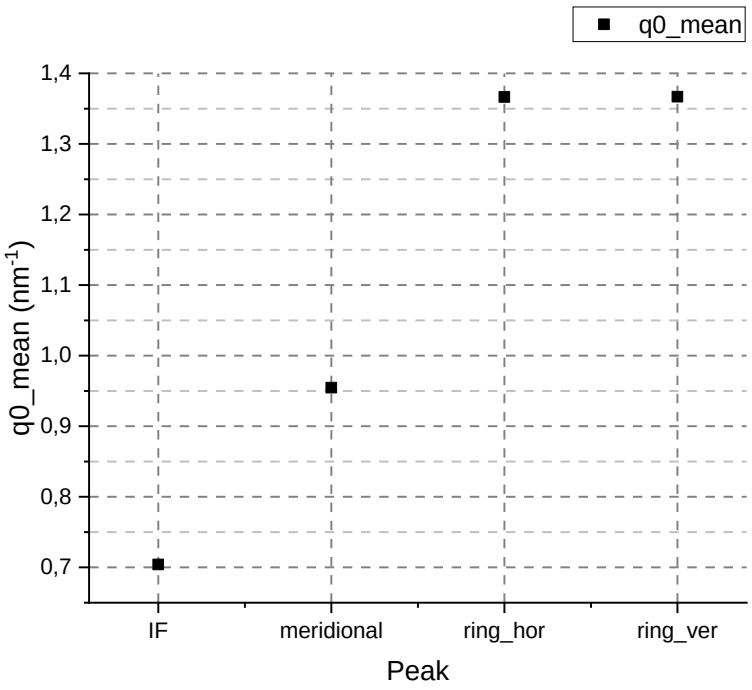

Figure 5.1: Means of peak positions q_0 of all six samples before first extension (unloaded); error bars smaller than symbols

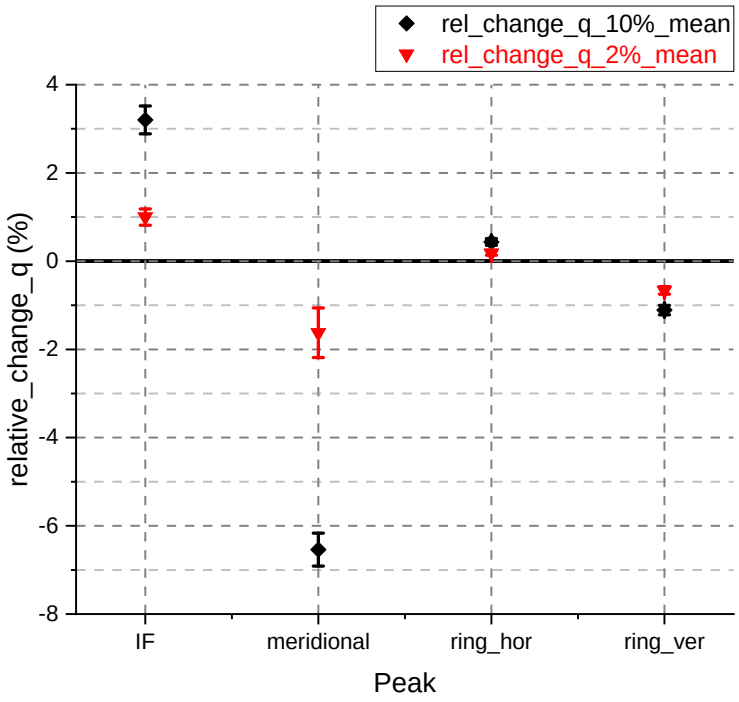

Figure 5.2: Relative changes of peak positions (in %): black diamonds for 10% strain and red triangles for 2% strain

	$\overline{q_0}$ (nm^{-1})	$\overline{d_0}$ (nm)	$\overline{\Delta q/q_0}$ (%) for 10% strain	$\overline{\Delta q/q_0}$ (%) for 2% strain
IF	0,7041 ± 0,0023	8,923 ± 0,029	+(3,20 ± 0,32)	+(1,00 ± 0,19)
meridional	0,9546 ± 0,0039	6,582 ± 0,027	−(6,54 ± 0,38)	−(1,62 ± 0,57)
ring_hor	1,367 ± 0,011	4,598 ± 0,015	+(0,434 ± 0,077)	+(0,184 ± 0,048)
ring_ver	1,3669 ± 0,0039	4,597 ± 0,013	−(1,11 ± 0,11)	−(0,664 ± 0,085)

Table 5.2: Average peak positions $\overline{q_0}$ in reciprocal space corresponding to positions $\overline{d_0}$ in real space as well as the relative changes of the peaks when the hair samples are subjected to mechanical strain.

matching structures in real space rise. These structures are orientated parallel to the hair axis and, therefore, parallel to the axis of tension. These findings are in accordance with the expectation that structures perpendicular to the load direction should decrease and structures orientated parallel to the load axis are supposed to increase.

The greatest change can be seen in the meridional arc, which decreases by 6,5% for a strain of 10% respectively by 1,6% for a strain of 2%. The IF peak increases by 3,2% for a strain of 10% and by 1% of a strain of 2%. The values of the ring peak change only slightly. Also, the difference between 2% and 10% strain is not that clearly. The values of the horizontal ring section rise by 0,4% for 10% strain respectively by 0,2% for 2% strain. The peak of the vertical ring sections declines by 1,1% for a strain of 10% and by 0,7% for a strain of 2%.

For comparing the results of different strain levels, it can be useful to calculated the portions of the macroscopic strain that are hold by the respective substructures of hair. For a macroscopic strain of 10%, these percentages are calculated by multiplying the relative changes of q-values in Table 5.2 by 10. For a strain of 2%, the percentages of the macroscopic strain are received by dividing by 2 and multiplying by 100. Hence, when hair is subjected to a macroscopic strain of 10%, the intermediate filaments take over 65% of this tension (indicated by the meridional peak q_m), resulting in a lateral decrease of the IF distance by 32% of the overall strain (evaluated via q_{IF}). Whereas, lipids that are orientated perpendicular to the tension axis ($q_{ring\ ver}$) only make up 11% of the macroscopic strain. Lipids that lay parallel to the axis of tension ($q_{ring\ hor}$) bear only 4% of the global strain.

Calculating the portions for a global strain of 2% gives an even greater percentage of tension taken over by the IFs. The increase of the axial staggering of molecules along the IFs bears 81% of the overall strain. The centre-to-centre distance of the

filaments decreases by 50% of the macroscopic strain. Lipid layers normal to the axis of tension make up for 33%. Lipids aligned parallel to the fibre axis share 9% of the global strain.

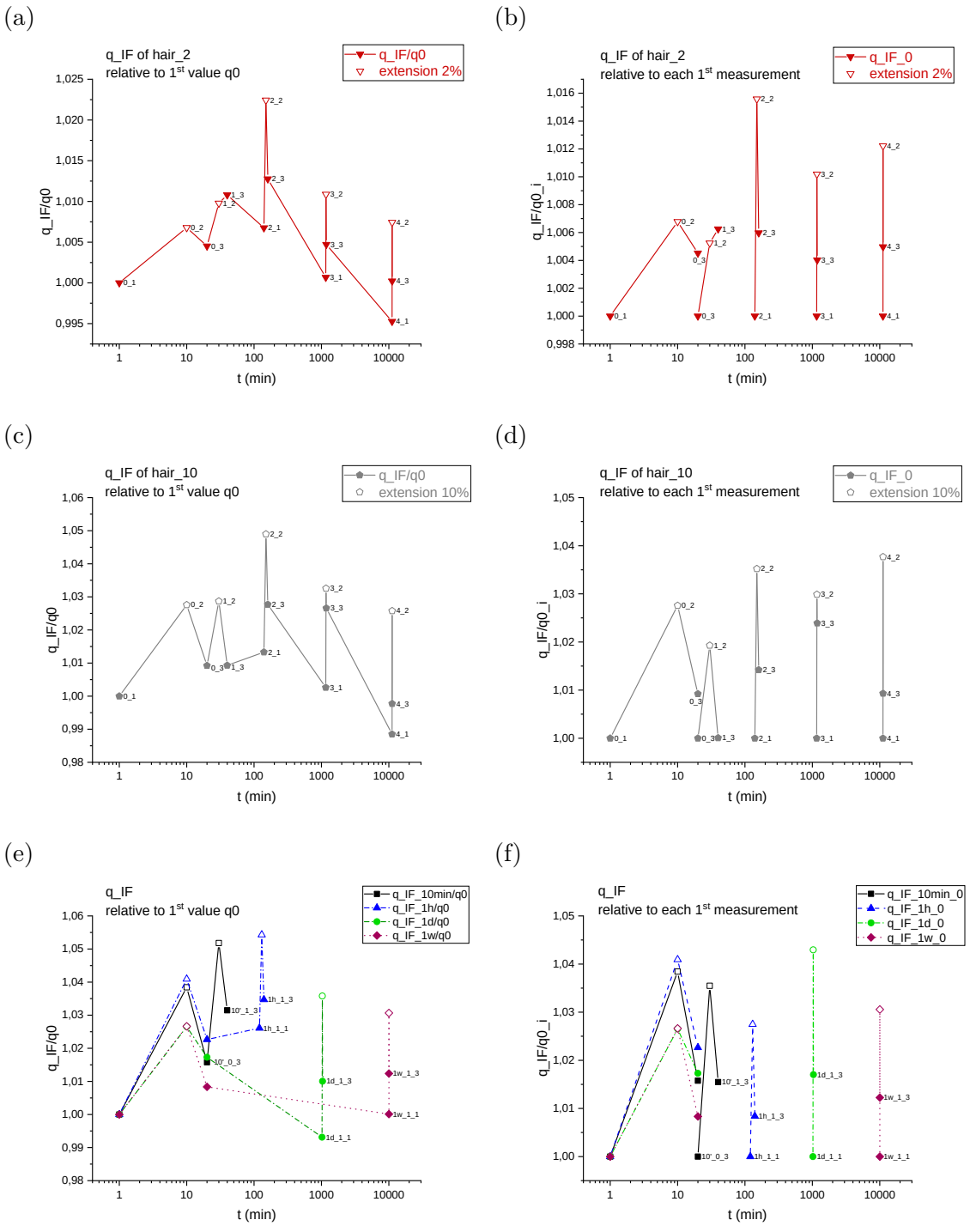

Figure 5.3: Positions of the IF peak for the whole measurement cycle: relative to the first measurement q_0 in the graphs on the left; relative to each first measurement of each cycle in the graphs to the right. Sample hair_2 at the top, hair_10 in the middle, the other four samples (hair_10min, hair_1h, hair_1day, hair_1week) at the bottom.

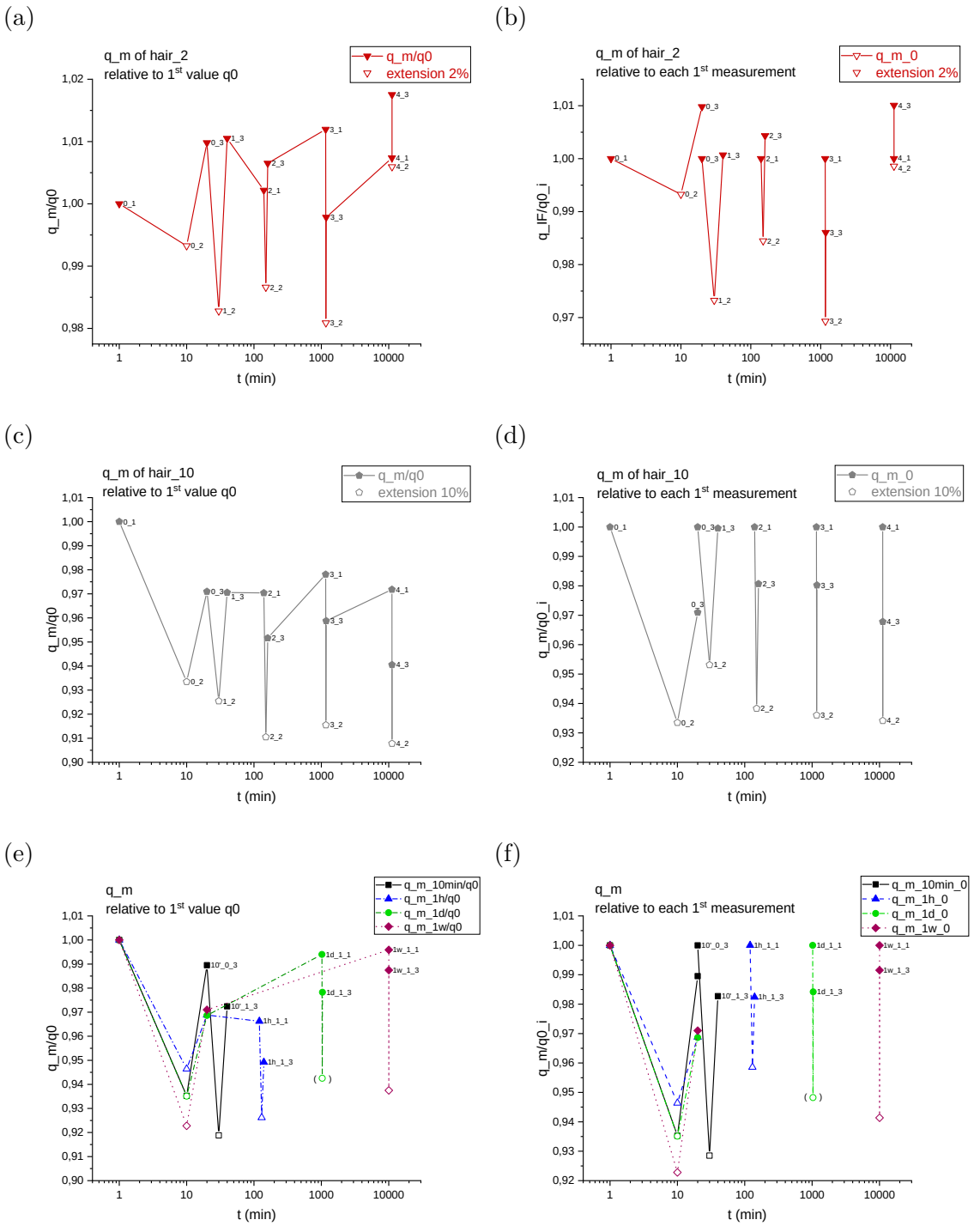

Figure 5.4: Positions of the meridional arc for the whole measurement cycle: relative to the first measurement q_0 in the graphson the left; relative to each first measurement of each cycle in the graphs to the right. Sample hair_2 at the top, hair_10 in the middle, the other four samples (hair_10min, hair_1h, hair_1day, hair_1week) at the bottom.

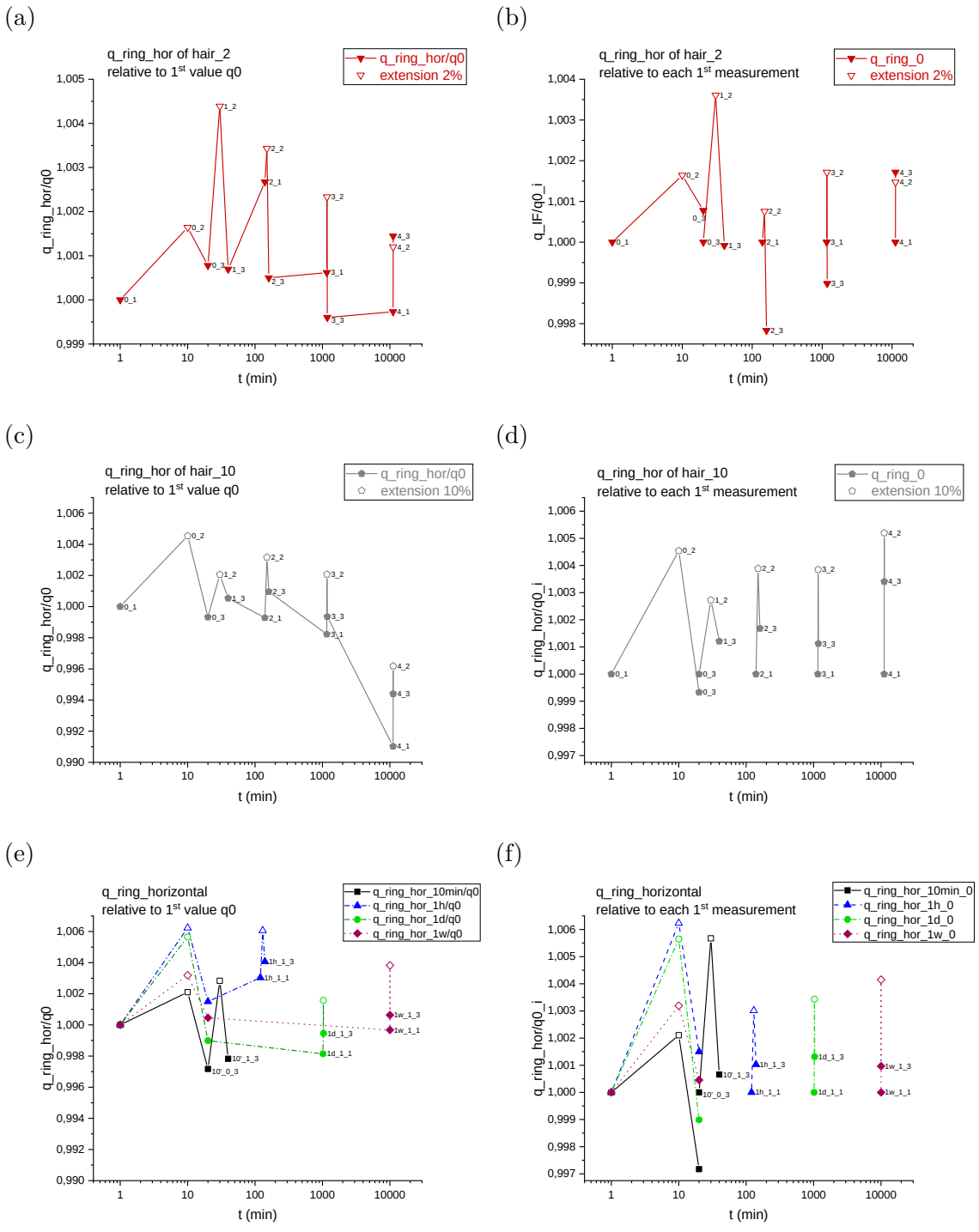

Figure 5.5: Positions of the horizontal ring peak for the whole measurement cycle: relative to the first measurement q_0 in th graphs on the left; relative to each first measurement of each cycle in the graphs to the right. Sample hair_2 at the top, hair_10 in the middle, the other four samples (hair_10min, hair_1h, hair_1day, hair_1week) at the bottom.

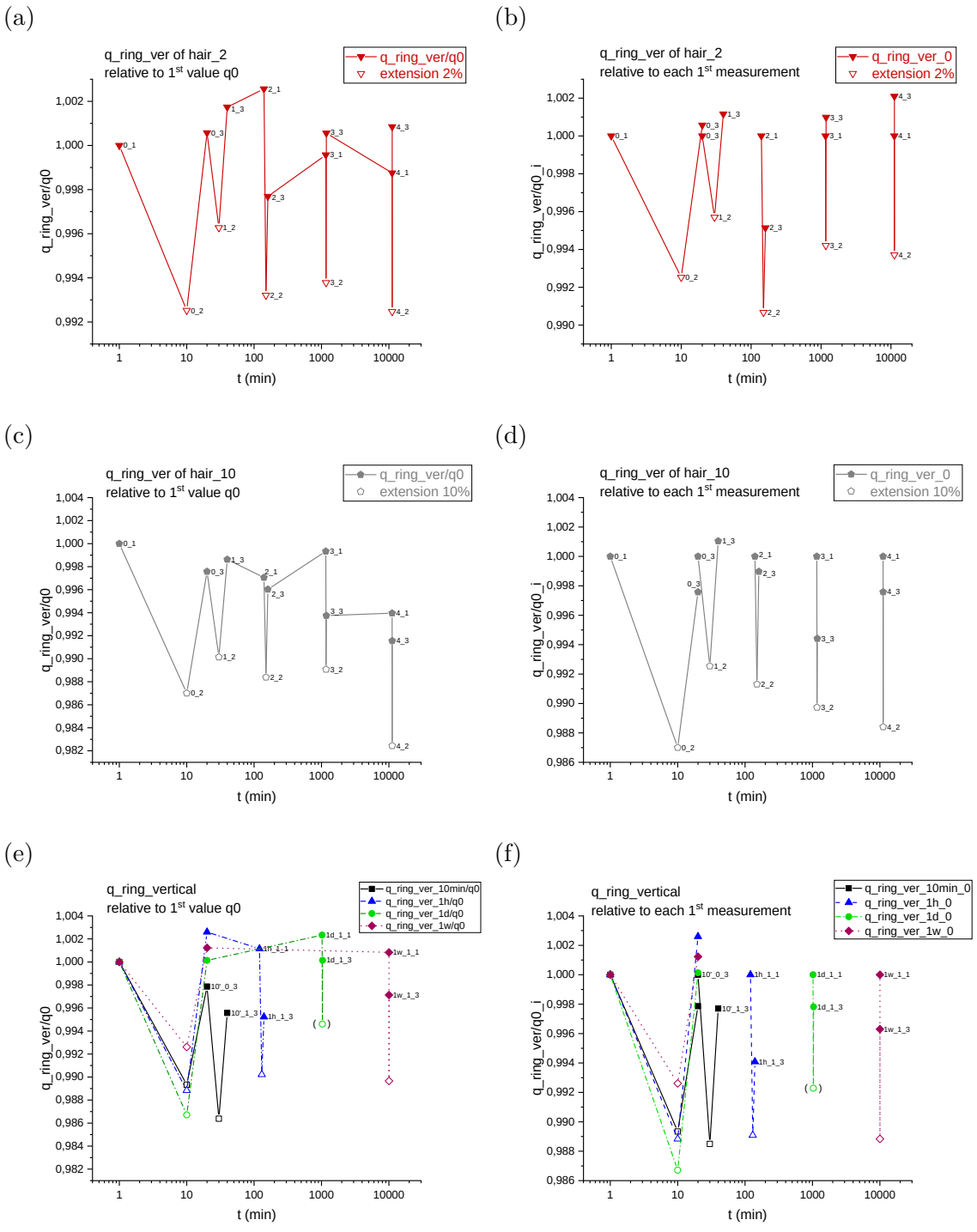

Figure 5.6: Positions of the vertical ring peak for the whole measurement cycle: relative to the first measurement q_0 in the graphs on the left; relative to each first measurement of each cycle in the graphs to the right. Sample hair_2 at the top, hair_10 in the middle, the other four samples (hair_10min, hair_1h, hair_1day, hair_1week) at the bottom.

6 Discussion

For any kind of interpretation of the outcome of the analysis, it is essential to remember that scattering data q and real space distances d in the specimen behave reciprocally. Peak positions of the scattered intensity at large q-values corresponds to small periodic structures in the sample and vice versa. Similarly, a decrease in q-values is caused by an increase of the correlated structure d in the hair sample. The latter relation is crucial for the analysis of changes that are caused by strain on the fibre. More precisely, we use the correspondence in Equation 4.5.4 to estimate relative changes in the specimen by the calculated relative changes of scattering positions q. That means, we assume that an increase of $p\%$ in reciprocal q-values corresponds to a decrease of approximately $p\%$ in real space distances d.

Considering the results of peak positions of virgin, unstrained hair in Table 5.2, the findings are in good agreement with values found in literature, cf. [3, pp. 109–111] or [4, p. 6]. Changes in the substructure of hair when exposed to mechanical strain are discussed according to the research questions stated in the introduction. Since these questions are central for the discussion, they are repeated here as a reminder:

i. How is mechanical strain divided on the substructures of the hair fibre?

ii. Does recovery take place? If yes, on which time scale does this happen?

iii. What is the effect of repeated straining?

iv. Is there a difference between pseudo-elastic (strains below approx. 2%) and pseudo-plastic (strains above 2%) deformation?

Ad i) Concerning the question, how mechanical strain is divided on the substructures of hair, one has to analyse the changes of peak positions when the specimen is strained. Average values of relative changes in q-values are calculated in Table 5.2 and visualized in Figure 5.2. What is striking, is the fact that there is a huge difference in the shift of average peak positions due to tensile strain for the respective reflections. The most pronounced change is observed for the meridional arc, corresponding to

the axial staggering of molecules along the IFs. For a macroscopic strain of 10%, this reflection changes by 65% of the overall strain. For a global strain of 2%, this portion is even larger with 81%. If one sees the axially staggered molecules as a probe for the strain of the IFs, this suggests that most of the global strain is taken over by the IFs. The lateral distance of IFs shrinks by 32% of the overall strain of 10% respectively by 50% of a global strain of 2%. Hence, for pseudo-plastic straining (10% strain), the transversal strain of the IFs is about half of the longitudinal strain, which suggests a Poisson's ratio at the nanoscale of 0,5, i.e., incompressibility. This is in coincidence with the macroscopic Poisson's ratio of hair of 0,5 (cf. [13, pp. 241–242]). Such behaviour is often observed for elastomers (cf. [14]).

Considering the results for the ring peak that corresponds to lipid layers, two main features are observed. Firstly, one notices that the nanoscopic strain in the lipids is nearly the same for macroscopic tensile strains of 2% and 10%. In both cases the change in the lipid layer distances is clearly smaller than the one observed for the IFs. Secondly, the ratio of transverse to longitudinal strain (corresponding to double lipid layers orientated parallel and perpendicular to the tensile strain) is difficult to measure and in the range of 0,3 - 0,4. The lipids are mainly present in the cuticle, which has a scale-like structure in human hair, similar to the scales of a fish. Therefore, one can imagine that for a high strain the scales separate from each other. This suggests a limit in the strain of lipids, which might be at approximately 1%.

Concluding, findings suggest that the intermediate filaments take over most of the strain. The huge increase in the axial staggering of molecules along the IFs indicates that the surrounding matrix plays only a minor role in the mechanical properties of hair. Also, other hierarchical structure elements do not seem to play a similar important role. An underlying mechanism, causing the major straining of the IFs, could be the unravelling of α-keratin helices. To prove this hypothesis, further investigation would be necessary. This could be done via WAXS (wide angle X-ray scattering). With this technique the size of α-keratin as well as of β-sheets could be measured. The latter is a different structure of keratin. In hair, α-helices transform to β-sheets when the fibre is subjected to large tensions. Investigation of the unravelling of α-helices has been performed e.g. by Kreplak et al. in [15]. Studies of the α-helix to β-sheet transformation by the same authors can be found in [16]. The β-sheet structure is supposed to occur only for strains above 20% or in conditions of at least 30% humidity. According to these assumptions, in the experiments carried out in this thesis, only an unravelling of the α-helices should have occurred. Additional information about keratin and its properties is available in the review on keratin by Wang et al. in [17].

When comparing the findings with studies of other biological fibres, one notices that hair behaves extraordinary. Typically, mechanical strain is divided rather equally on the subcomponents of hierarchically structured tissues. However, for hair this is not the case, but the intermediate filaments show a nanoscopic strain of approx. two thirds of the global strain. So far, this is an outstanding result for biological tissues. One can, for instance, compare the findings with those of tendons, which are also hierarchically structured. Their basis component is collagen. Fratzl, Misof and Zizak investigated the mechanical behaviour of collagen in a rat tail tendon. They noticed that the nanoscopic strain accounts for 40% of the global tension (cf. [18, p. 121]). In this case other structures, such as a surrounding matrix, take over remaining portions of the macroscopic strain. Similarly, Gupta et al. analysed the strain on substructures in bone (precisely, of bovine femoral bone). The evaluation showed that fibrils take over 41% of the macroscopic strain (cf. [19, p. 17741]). These findings for other biomaterial underline how striking the results for hair are and that the huge increase of the axial staggering of molecules in the intermediate filaments, when the hair is strained, is an outstanding process for hierarchically structured tissues.

From the outcomes of the evaluation, a basic model of straining hair is proposed, taking into account the changes in various substructures. This model is schematically visualised in Figure 6.1. To enhance readability, the increase of all substructures is visualised ten times larger than it would actually happen for a global strain of 10%. Otherwise the changes would hardly be visible.

In subfigure 6.1a the unstrained hair fibre is depicted. The lipid layers, shown in red, are assumed to be located in the cuticle, the outermost part of the hair. The layer distance is marked by d_{ring}. The most important substructure when it comes to straining are the intermediate filaments. They can be approximated as infinite long cylinders. Their centre-to-centre distance is marked in green (d_{IF}), the axial staggering of molecules in blue (d_m). The cortical cells (in brown) and the macrofibrils (in light grey) are assumed to play negligible roles in the mechanical behaviour of hair. The resulting changes in the substructure, when tension is applied along the hair axis, are displayed in subfigure 6.1b. The vast majority of the global strain is taken over by the IFs, resulting in a significant increase of the axial staggering distance and a decrease in the lateral IF distance. The lipids show only minor changes in their size. Instead, their relative position on the hair is unchanged, meaning that the space between neighbouring lipids increases, when the hair is strained.

This simple straining model, however, does not explain the underlying processes on molecular level. Also, it would be interesting to understand the interaction between

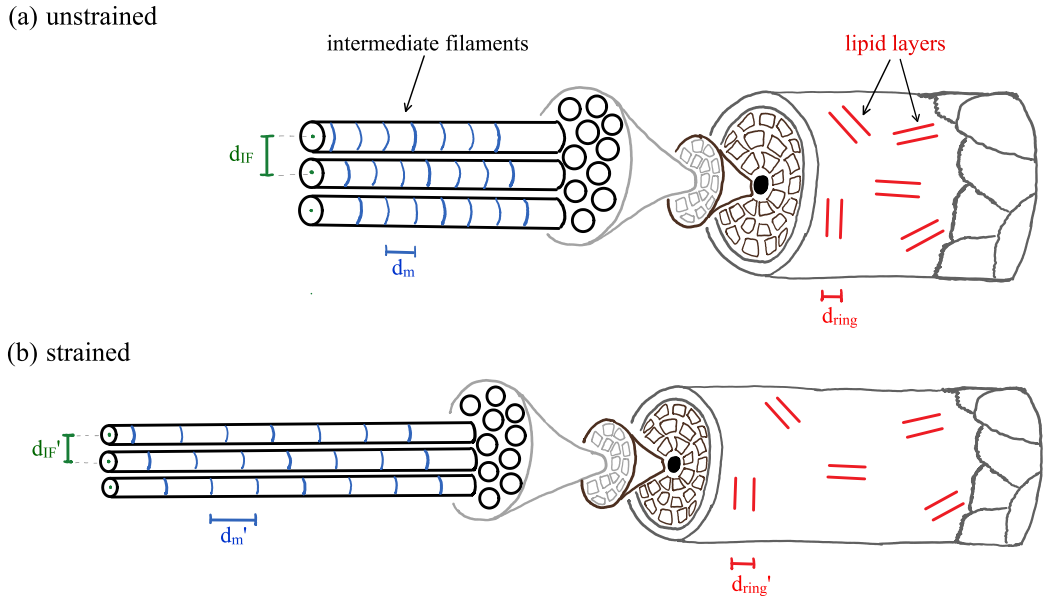

Figure 6.1: Proposed model of straining hair: Intermediate filaments as black cylinders with centre-to-centre distance d_{IF} resp. d'_{IF} in green, axial staggering d_m resp. d'_m in blue, lipids with layer distance d_{ring} resp. d'_{ring} in red. Unstrained hair in (a), strained hair in (b). The changes in size are depicted ten times larger than actually the case for a strain of 10%.

the intermediate filaments and the surrounding matrix. Concerning these questions, Kreplak et al. proposed a deformation model of hard α-keratin fibres in [20]. They found that on the one hand a stretching of the keratin molecules occurs and that on the other hand those molecules slide inside the filaments, when hair is subjected to mechanical tension. Our results show that stretching on the nanoscale is dominant and accounts for two thirds of the macroscopic strain.

Ad ii) In order to analyse whether recovery takes place and on which time scale that might happen, the first and second measurement cycle of each specimen are compared. The most precise results are available for the specimens hair_10min, hair_1h, hair_1day and hair_1week, since they were all only strained twice. The relevant peak positions of these specimens (relative to the first measurement) are presented in subfigures 5.3e - 5.6e. Analysing the first tension cycles of these specimens (with the first SAXS measurement 0_1 at load 0, the second SAXS measurement 0_2 at load 10% and the third one 0_3 at load 0 again) gives the same findings for all four peaks: The third peak position is different from the first one, which means that a plastic deformation occurs. For the lateral IF distance q_{IF} and the meridional arc q_m, this plastic deformation is roughly one third of the change between the original (0_1)

and the strained values (0_2). Comparing the first and the second load cycle for the lateral IF peak, gives the following observation. Successive cycles of hair_10min and hair_1h differ from the first cycle, whereas they are nearly identical to the respective first cycle for hair_1day and hair_1week, that is, for waiting periods of approximately 1 day and 1 week. Within these longer time spans the peak position q_{IF} returned to its original value (compare the first SAXS measurement 1_1 of the second load cycle with the original value 0_1). Hence, it is clearly visible that recovery of the nanoscopic structure takes place. The time necessary for the underlying self-healing processes seems to measure between 100 min and 1 day.

Recovery is also visible to a lesser extent for the meridional arc in subfigure 5.4e. For this reflection, the differences between the four specimens are not as apparent as for the lateral IF peak. For lipids, recovery can not be unambiguously verified, because the observed values as well as the changes in peak positions are rather small.

It can be speculated that for relaxation the matrix plays an important role, since the effect is more pronounced for the IF distance than for the meridional arc. After the release of the tension on the hair, the meridional arc seems to return faster to its original value than the lateral IF peak does. This suggests that the intermediate filaments act as elastic fibres in a matrix with non-Newtonian viscosity. These fibres are expected to be covered by the cuticle with lipid rich scales.

Ad iii) For evaluating the effects of repeated straining, results of sample hair_10 that was in total strained five times is compared to the specimens strained twice, that is, hair_10min, hair_1h, hair_1day and hair_1week. This is performed via comparing the subfigures 5.3c - 5.6c of specimen hair_10 to the figures 5.3e - 5.6e of the other four samples. For analysing the patterns within each load cycle, one looks at the subfigures 5.3d - 5.6d for hair_10 resp. subfigures 5.3f - 5.6f for the samples strained twice.

Taking all the errors of measurements into account, there seems to be little difference between single and repeated straining. Different load cycles of hair_10 show similar results when compared with one another as well as when compared to the load cycles of the respective specimens hair_10min to hair_1week, which were only strained twice. Hence, repeated straining seems to be little problem for hair.

Small changes are visible for the lateral IF peak. From the results, it can be speculated that the matrix between the intermediate filaments is composed of an amorphous substance with non-Newtonian viscosity. When strained once, it seems to behave rather elastically. Repeated straining, however, has probably a persisting effect on the matrix. Possibly, a separation and clumping of the matrix material

occurs after several load cycles.

Ad iv) Last but not least, pseudo-plastic and pseudo-elastic straining is compared. This is performed by studying the results of hair_10 strained by 10% and hair_2 strained by 2%. Results of the latter sample are visible in subfigures 5.3a - 5.6a and 5.3b - 5.6b. Both samples are subjected to the same measurement procedure. Unfortunately, findings for hair_2 have to be taken with caution, because for some of the data points, the magnitude of straining effects is of similar dimension as the uncertainty of the data. For more precise data, additional experiments carried out with a synchrotron would be necessary.

Generally, the results for the specimen strained in the pseudo-elastic region show the same pattern as hair strained pseudo-plastically. Peak positions increase resp. decrease, when the specimen is subjected to tension. When the strain is released the positions drop back closely to their original value, but often a slight deviation remains. During the waiting periods the q-values show a tendency to recover. Interestingly, a strain of 2% does not show a solely elastic behaviour. Instead, pseudo-plastic changes occur and recovery mechanisms take place.

Hence, no clear differences between hair strained by 10% and by 2% are visible in the recovery behaviour. As already described for question i, a strong difference is found in the ratio of nanoscopic to macroscopic strain (see Table 5.2). The straining of the IFs yields different values for pseudo-plastic and pseudo-elastic straining, but only a small difference in strain values of the lipids is visible. The reason is again the large nanoscopic strain in the intermediate filaments, whereas the scales in the cuticle exhibit an upper strain limit of about 1%.

7 Conclusion

As hair plays an important role in beauty, the cosmetic industry is interested in developing various hair care and styling products. For best results, it is essential to understand the properties of natural hair. Only with this knowledge, effects of hair treatment can be analysed properly. In daily life, hair is subjected to several environmental impacts. One of them is being subjected to mechanical stress. This occurs for example via stroking, weaving braids, curling or straightening hair, to name just a few.

The aim of this thesis was to analyse the mechanical properties of natural human hair. Besides investigating, how tensile strain effects different substructures of hair, a special focus was put on the recovery behaviour. For this purpose an appropriate measurement cycle was designed. Different samples were strained repeatedly with varying waiting periods in between the tensile tests and the nanostructure was analysed via small angle X-ray scattering (SAXS).

One of the main results of this thesis is that human hair displays an extraordinary behaviour among hierarchically structured tissues, as far as the division of strain on the subcomponents is concerned. Typically, global tension is divided rather equally on the substructures, as it is, for instance, the case for collagen in tendons and bones (cf. [18], [19]). However, hair behaves differently. For this fibre, the vast majority of the macroscopic strain is taken over by a single subcomponent. The so-called intermediate filaments (IFs) bear 65% (for pseudo-plastic straining) to 81% (for pseudo-elastic straining) of the global strain. The transversal to longitudinal strain ratio of the IFs, i.e., Poisson's ratio at the nanoscale, is approximately 0,5. This indicates that the IFs show an incompressible behaviour. As this is in coincidence with the macroscopic Poisson's ratio (cf. [13, pp. 241–242]), this suggests that the intermediate filaments take over the main portion of the global strain and other substructures of hair play negligible roles for the mechanical properties. For the lipids, only clearly smaller strains are observed. The difference between strain values for a global strain of 2% and of 10% is very small. Since the lipids are mainly located in the cuticle, it is assumed that the scales of hair separate from each other when subjected to high tensile

strains. Hence, the scales as well as the lipids show an upper strain limit of about 1%.

When it comes to recovery, the results show that the nanostructure of hair does show full recovery after being subjected to tensile strain. The time necessary for recovery was shown to be longer than 100 minutes, but shorter than 1 day. Repeated straining seems to be little problem for hair and recovery does still take place.

The effect of recovery was most pronounced for the lateral IF peak. From this result, it can be speculated that the amorphous matrix between the intermediate filaments plays an important role in the recovery behaviour. A possible explanation is that this matrix shows a non-Newtonian viscosity. When strained once, this matrix might behave rather elastically, but starts clumping together when strained several times. However, so far this is mainly speculation. Additional experiments would have to be designed to investigate the molecular processes when hair is subjected to tensile strain.

Concluding, these findings suggest that the mechanical properties of hair are mainly dominated by the intermediate filaments. These behave as elastic fibrils surrounded by an amorphous matrix with non-Newtonian viscosity. The hair is covered by the cuticle whose outermost cover are lipid-rich scales that separate from each other under high tensile strains. The nanostructure of hair recovers from tensile strain within a time span of 100 min to 1 day.

The outcomes of this thesis provide basic informations about mechanical properties of natural human hair and its recovery behaviour. In future studies, additional details can be investigated. On the one hand, it would be interesting to examine the effects of straining on the molecular level. Experiments should be designed to analyse the processes taking place in the matrix and within the IFs when hair is strained. On the other hand, one could aim to further investigate the precise time span that is necessary for full recovery. Here, the focus should be put on waiting periods between 100 minutes and 1 day.

Furthermore, findings of this thesis can serve as a reference for future studies performed with hair that has been subjected to a certain treatment with caring or styling products. Questions that could be investigated are for example, how hair colouring and other styling techniques effect the mechanical properties of hair. Moreover, further research could be carried out to determine whether care products can be developed that improve the mechanical properties of hair and its capability to recover.

Abstract

In this master thesis, mechanical properties of natural human hair are analysed in-situ via mechanical loading at the macroscale and small angle X-ray scattering (SAXS) measurements at the nanoscale. The mechanical quality of hair is important for the cosmetic industry, because mechanical stress is applied to hair on a regular basis for instance via stroking, tying the hair into a ponytail or straightening it. It is desired that such actions do not damage the hair. Ideally, for hair treatments, the structure should be conserved or changes should be reversible.

We subjected strands of human hair to tensile stress and measured SAXS patterns to follow the nanostructure in-situ. Three reflections are identified, which give information on the distance of intermediate filaments (IFs), on the strain in these filaments (meridional peak from axially staggered molecules), and on the deformation behaviour of the cuticle (lipid ring describing the distance of double lipid layers in load direction and perpendicular to it).

It turned out that the nanoscopic strain of the IFs is very high: It is about two third of the macroscopic strain, which leads to the conclusion that the IFs take over nearly all the mechanical load. The distance between the IFs allows to calculate the ratio transversal to longitudinal strain (Poisson's ratio at the nanoscale), which gives a number of about 0,5. This is in coincidence with the macroscopic Poisson's ratio. A value of 0,5 is often observed for elastomers and described as incompressibility of the material. As the Poisson's ratio at the nanoscale is identical to the one at the macroscopic scale, one can conclude that further hierarchical levels in the material such as macrofibril boundaries or the cell membrane complex have no significant effect on the mechanical properties. Only a small nanoscopic strain of about one per cent was observed for the lipid layers: As they are mainly located in the scales of the cuticle, this indicates that the scales shift against each other under high strain, which leads to an upper strain limit for the lipid layers. A recovery of the structure for certain waiting periods after an initial load cycle could be observed. The structure in successive load cycles with waiting periods of 10 min and 1 hour in between the cycles differs from the one in the first load cycle, but returns to its original value after a waiting period of 1 day or 1 week. The conclusion is that between 1 hour

and 1 day, a relaxation of the structure takes place.

Further research will more precisely determine the time range of the recovery of material properties. Additionally, experiments have to be designed, which could clarify the molecular origin of the observed relation of structure and mechanical properties.

Zusammenfassung

In dieser Masterarbeit werden die mechanischen Eigenschaften von menschlichem Haar in-situ durch mechanische Belastung auf der Makroebene und durch Röntgenkleinwinkelstreuung (SAXS) auf der Nanoebene analysiert. Für die Kosmetikindustrie sind diese Eigenschaften von Relevanz, da Haare im Alltag regelmäßig mechanischen Belastungen ausgesetzt sind. Dies findet etwa durch Kämmen, durch Zusammenbinden der Haare zu einem Zopf oder durchs Haare Glätten statt. Solche Tätigkeiten sollen die Haare nicht beschädigen. Falls es zu Veränderungen kommt, so ist es erwünscht, dass diese reversibel sind.

Es werden Zugversuche an Haarproben durchgeführt und SAXS-Streubilder aufgenommen, um die Nanostruktur in-situ zu beobachten. Drei Reflexe werden analysiert, die Informationen zum Abstand der Intermediärfilamente (IFs) geben sowie zur Dehnung dieser Filamente (meridionaler Bogen, der von in Längsrichtung zueinander versetzter Moleküle stammt) und dem Deformationsverhalten der Kutikula des Haares (Lipidring, der die Abstände von Doppellipidschichten in Lastrichtung und normal dazu beschreibt).

Es zeigte sich, dass die nanoskopische Dehnung der IFs mit etwa zwei Dritteln der makroskopischen Dehnung sehr hoch ist. Dies führt zu der Schlussfolgerung, dass die IFs nahezu die gesamte mechanische Last aufnehmen. Unter Bezugnahme auf den Abstand der IFs kann das Verhältnis von transversaler zu longitudinaler Dehnung berechnet werden (Poissonzahl auf Nanoebene). Mit einem Wert von etwa 0,5 stimmt dies mit der makroskopischen Poissonzahl überein. Ein Wert von 0,5 wird häufig bei Elastomeren beobachtet und entspricht einem inkompressiblen Material. Da die Poissonzahl auf Nanoebene ident ist zu jener auf Makroebene, liegt der Schluss nahe, dass andere hierarchische Level wie die Makrofibrillen oder der Zellmembrankomplex keinen wesentlichen Einfluss auf die mechanischen Eigenschaften von Haar haben. Für die Lipide wurde nur eine geringe nanoskopische Dehnung von etwa einem Prozent beobachtet. Nachdem die Lipide hauptsächlich in den Schuppen des Haares in der Kutikula vorkommen, weist dies darauf hin, dass sich die Schuppen bei hoher Dehnung gegeneinander verschieben. Daraus resultiert weiters eine obere Grenze für die Dehnung der Lipide.

Es wurde eine Regeneration der Struktur nach einer gewissen Wartezeit nach einem ersten Belastungszyklus festgestellt. Bei Wartezeiten von 10 Minuten und einer Stunde zwischen aufeinander folgenden Lastzyklen unterschieden sich die beobachteten Werte der beiden Zyklen. Betrug die Wartezeit jedoch einen Tag oder eine Woche, so wurden ähnliche Werte wie im ersten Zyklus beobachtet. Daraus kann geschlossen werden, dass die nötige Zeit für die Rückbildung der Nanostruktur zwischen einer Stunde und einem Tag liegt. Um diese Zeitspanne weiter einzugrenzen, sind weitere Untersuchungen notwendig. Des Weiteren sollten Experimente geplant werden, mit Hilfe derer die molekularen Ursachen für die beobachteten Effekte bei mechanischer Belastung geklärt werden können.

Bibliography

[1] J. D. dos Santos, H. G. M. Edwards and L. F. C. de Oliveira. „Raman spectroscopy and electronic microscopy structural studies of Caucasian and Afro human hair“. eng. In: *Heliyon* 5.5 (2019).

[2] C. Popescu and H. Höcker. „Hair—the most sophisticated biological composite material“. eng. In: *Chem. Soc. Rev.* 36 (8 2007), pp. 1282–1291.

[3] T. H. Semmence. „Characterisation of α-Keratin Fibres“. eng. PhD thesis. Imperial College London, Aug. 2018.

[4] A. R. M. Müllner et al. „Porosity at different structural levels in human and yak belly hair and its effect on hair dyeing“. eng. In: *Molecules* 25.9 (2020).

[5] B. D. Cullity. *Elements of X-ray diffraction*. eng. 3. ed., 4. print. Upper Saddle River, NJ [et al.]: Prentice Hall, 2001.

[6] R. J. Roe. *Methods of x-ray and neutron scattering in polymer science*. eng. Topics in polymer science. New York, NY [et al.]: Oxford Univ. Press, 2000.

[7] I. W. Hamley. *Small-angle scattering : theory, instrumentation, data, and applications*. eng. Hoboken, NJ: Wiley, 2021.

[8] H. Schnablegger and Y. Singh. *The SAXS Guide*. eng. Graz: Anton Paar GmbH, 2013.

[9] R. Gross. *Festkörperphysik*. ger. 3. ed. De Gruyter Studium. Berlin Boston: De Gruyter, 2018.

[10] L. Spieß et al. *Moderne Röntgenbeugung: Röntgendiffraktometrie für Materialwissenschaftler, Physiker und Chemiker*. ger. 3. ed. Wiesbaden: Springer Fachmedien Wiesbaden, 2019.

[11] T. Freltoft, J. K. Kjems and S. K. Sinha. „Power-law correlations and finite-size effects in silica particle aggregates studied by small-angle neutron scattering“. eng. In: *Phys. Rev. B* 33 (1 Jan. 1986), pp. 269–275.

[12] F. Briki, B. Busson and J. Doucet. „Organization of microfibrils in keratin fibers studied by X-ray scattering: Modelling using the paracrystal concept“. eng. In: *Biochimica et Biophysica Acta - Protein Structure and Molecular Enzymology* 1429.1 (1998), pp. 57–68.

[13] J. Lee and H. J. Kwon. „Measurement of stress–strain behaviour of human hair fibres using optical techniques“. eng. In: *International Journal of Cosmetic Science* 35.3 (2013), pp. 238–243.

[14] G. N. Greaves et al. „Poisson's ratio and modern materials“. eng. In: *Nature materials* 10.11 (2011), pp. 823–837.

[15] L. Kreplak, J. Doucet and F. Briki. „Unraveling double stranded α-helical coiled coils: An x-ray diffraction study on hard α-keratin fibers“. eng. In: *Biopolymers* 58.5 (2001), pp. 526–533.

[16] L. Kreplak et al. „New Aspects of the α-Helix to β-Sheet Transition in Stretched Hard α-Keratin Fibers“. eng. In: *Biophysical journal* 87.1 (2004), pp. 640–647.

[17] B. Wang et al. „Keratin: Structure, mechanical properties, occurrence in biological organisms, and efforts at bioinspiration“. eng. In: *Progress in Materials Science* 76 (2016), pp. 229–318.

[18] P. Fratzl et al. „Fibrillar Structure and Mechanical Properties of Collagen“. eng. In: *Journal of structural biology* 122.1-2 (1998), pp. 119–122.

[19] H. S. Gupta et al. „Cooperative Deformation of Mineral and Collagen in Bone at the Nanoscale“. eng. In: *Proceedings of the National Academy of Sciences - PNAS* 103.47 (2006), pp. 17741–17746.

[20] L. Kreplak et al. „A New Deformation Model of Hard α-Keratin Fibers at the Nanometer Scale: Implications for Hard α-Keratin Intermediate Filament Mechanical Properties“. eng. In: *Biophysical Journal* 82.4 (2002), pp. 2265–2274.

List of Figures